TOPICAL REVIEW

Intense-field many-body S-matrix theory

A Becker[1] and F H M Faisal[2]

[1] Max-Planck-Institut für Physik komplexer Systeme, Nöthnitzer Str 38, D-01187 Dresden, Germany
[2] Fakultät für Physik, Universität Bielefeld, Postfach 100131, D-33501 Bielefeld, Germany

E-mail: abecker@mpipks-dresden.mpg.de and ffaisal@physik.uni-bielefeld.de

Abstract
Intense-field many-body S-matrix theory (IMST) provides a systematic *ab initio* approach to investigate the dynamics of atoms and molecules interacting with intense laser radiation. We review the derivation of IMST as well as its diagrammatic representation and point out its advantage over the conventional 'prior' and 'post' expansions which are shown to be special cases of IMST. The practicality and usefulness of the theory is illustrated by its application to a number of current problems of atomic and molecular ionization in intense fields. We also present a consistent S-matrix formulation of the quantum amplitude for high harmonic generation (HHG) and point out some of the most general properties of HHG radiation emitted by a single atom as well as its relation to coherent emission from many atoms. Experimental results for single and double (multiple) ionization of atoms and the observed distributions of coincidence measurements are analysed and the dominant mechanisms behind them are discussed. Ionization of more complex systems such as diatomic *and* polyatomic molecules in intense laser fields is analysed as well using IMST and the results are discussed with special attention to the role of molecular orbital symmetry and molecular orientation in space. The review ends with a summary and a brief outlook.

Contents

1. Introduction

The interaction of light with matter has been a fundamental topic in the history of quantum theory and as such has been studied now for a century. The recent upsurge of activity in studying the response of quantum systems (atoms, molecules, clusters, solids) subjected to strong electromagnetic radiation is a consequence of the availability of very intense and stable laser systems with high repetition rates in the laboratory. Currently, frequencies of available lasers range from the far-infrared through the optical up to the vacuum-ultraviolet and the soft x-ray regions. The focused laser intensity increased rapidly in the sixties and the seventies and then once again from the late eighties, thanks to a new amplification technique called 'chirped pulse amplification (CPA)' [147]. This has allowed unprecedented levels of light intensities of the order of 10^{20} W cm^{-2} or above to be generated in the laboratories, e.g. with Ti-sapphire laser systems. The field strength at these intensities is of the order of a teravolt per centimetre, i.e. a hundred times the strength of the Coulomb field that binds the ground state electron in the hydrogen atom[3]. As the focused laser intensities increased, the pulse lengths correspondingly decreased from the nanosecond (10^{-9} s) regime to the femtosecond (10^{-15} s) regime; very recently even sub-femtosecond pulses have been generated in the laboratory [157, 162, 88]. Since the availability of laser radiation in the sixties, new research fields of nonlinear optics and laser physics have emerged and new branches of technological research such as in fibre optics, tele-communications, material sciences, plasma physics, thermonuclear fusion, medicine etc have flourished. Simultaneously in the field of basic research, it led to

---

[3] The atomic unit of electric field strength is the field felt by an electron in the ground state of atomic hydrogen, $E_a = e/a_0^2 \simeq 5.1 \times 10^9$ V cm^{-1}, and the corresponding intensity is $I_a = 3.51 \times 10^{16}$ W cm^{-2}.

the discovery of novel aspects of light–matter interaction at the atomic level. Among them are the observation and interpretation of phenomena such as virtual absorption, multiphoton ionization, above-threshold-ionization, high harmonic generation, laser-induced electron correlation, laser-induced (optical) tunneling, Coulomb explosion etc. In this review, we shall limit ourselves to the discussion of a unified theoretical tool, called 'intense-field many-body S-matrix theory' (or IMST), for theoretical investigation of such highly non-perturbative phenomena, and discuss its application to some of the major experimental observations of which ionization of atoms and molecules is the most ubiquitous in intense laser fields.

2. Theoretical approaches to processes in intense laser fields

In intense light fields not only the usual photoionization by absorption of a photon of energy greater than that of the ionization threshold can take place but also by absorption of any number of photons. In fact, for a sub-threshold photon energy, a *multiphoton* ionization takes place in which an atom or a molecule is ionized by *virtual* absorption of more than one or many photons until a real (stationary) state is reached in the continuum when finally the overall energy–momentum conservation in the transition process is satisfied. In general, in very intense fields ionization can take place for laser photons of *any* energy and polarization. Also, the actual number of photons absorbed can be even larger than the minimum required for the energy conservation. In the latter event, the photoelectron energy spectrum shows a series of 'peaks' separated by the energy of a laser photon. This process is popularly known as the 'above-threshold ionization' (or ATI) and was first observed by Agostini *et al* in 1979 [1]. Its observation actually marked the breakdown of perturbation theory. The breakdown intensity for the lowest non-vanishing order perturbation theory (or LOPT) occurs e.g. for near optical wavelengths for intensities above about $I \simeq 5 \times 10^{12}$ W cm^{-2} [55].

In the *non*-perturbative intensity domain 'exact' calculations of the ionization probability can be made by direct numerical integration of the three-dimensional Schrödinger equation for effective one-electron (or hydrogenic) atoms or ions coupled to the laser field. For the *ab initio* numerical simulations of a system with N_e electrons, obviously one needs to solve a set of $3 \times N_e$, $N_e = 1, 2, 3 \ldots$, dimensional *partial* differential equations over a large spacetime grid. With the increase of the electron number beyond 2, this becomes prohibitive even with the currently available high power computers. So far, numerical simulations have been made mostly within the effective single-active-electron (SAE) model (e.g. [119, 149, 156]), in which the electrons are assumed to be effectively independent and only one electron that ionizes is considered to be 'active' (the remaining electrons are frozen in their initial configuration). Considerable progress towards numerical solutions of the six-dimensional Schrödinger problem for the double ionization, where two electrons can be 'active', has recently been made using state-of-the-art computations [160, 150, 161].

A second *ab initio* method of calculation is based on the Floquet theorem (e.g. [55]). It makes use of the assumed periodicity of electron-field interaction in time. In this method, the time-dependent Schrödinger equation is transformed into a set of time-independent radial coupled equations, which are solved either more directly by integrating the set of coupled equations numerically with appropriate boundary conditions [44], or by expansion of the stationary Floquet wavefunction in L^2-basis functions (e.g. [36, 133, 178, 179]). *Ab initio* Floquet calculations have been used to study a number of single-active-electron processes in atoms such as above-threshold ionization, laser-induced recombination and the so-called 'adiabatic stabilization' phenomenon. We refer the reader to two recent reviews [97, 37] which describe the method including its extension to many-electron systems as R-matrix theory, and its applications.

An alternative *ab initio* approach is a systematic approximation method for intense-field problems given by the IMST. S-matrix theories are well known in collision physics (e.g. [96, 134]). In its simplest version as the time-dependent perturbation theory (first given by Dirac), it has been widely used for investigation of laser-matter interaction problems in the early days of multiphoton physics (see e.g. [55]). Structurally, the usual S-matrix expansions are based on a single partition of the total Hamiltonian of the system into an unperturbed reference Hamiltonian and the 'interaction potential', which in the usual case is the laser-atom interaction Hamiltonian. Such a 'one-potential' scheme is not very useful for the analysis of strong-field processes, in which the internal Coulomb interaction between the charged particles in the atom or molecule, and the external laser-atom interaction energy are of comparable strength. The earliest forms of S-matrix theories which accounted *non-perturbatively* for the intense-field interaction, are typified by the well-known Keldysh–Faisal–Reiss (KFR) model [100, 53, 181], where the interaction with the laser field is emphasized. More generally, one needs to incorporate (a) the Coulombic interaction, (b) the laser interaction and (c) any intermediate (virtual) rearrangement Hamiltonian, on an equal footing. Thus, one requires to be able to account simultaneously of the *different* reference Hamiltonians in the initial and the final states, as well as the internal rearrangement Hamiltonian of the many-electron system (that can and does often occur in the intermediate states of the system) in intense fields. To account for these three possibilities simultaneously and systematically, a more general S-matrix expansion scheme, the so-called IMST, has been developed [65, 16]. It provides an effective method for analyses of direct or rearrangement processes that can occur in the presence of intense laser fields (or more generally for any reaction process and not necessarily in a laser field).

Formally, IMST may be thought of as a thorough rearrangement of the usual S-matrix series in such a way as to bring forward for the purpose of analysis any feature of interest in a transition process in the first few *leading* terms of the series. Then it proceeds systematically with the resulting series. Like virtually all S-matrix series, the IMST series is in all probability an asymptotic series. As such, often a knowledge of only the first few terms of the series can suffice to obtain an appropriate estimate. Here, we need not enter into the discussion of various methods of estimating the sum of an asymptotic series from the knowledge of its first few terms, but for the interested readers, we merely mention the various Padé-schemes and the Shank-transformations (e.g. [25]) for effecting them, if needed; an example of application of the latter scheme is shown in [61].

We point out that besides being able to provide a quantitative estimate of relevant transition probabilities, IMST can qualitatively identify possible 'mechanisms' involved in a given process of interest by explicitly making use of and interpreting the Feynman-like diagrams that are automatically generated by the series. Identification of a dominant 'mechanism', or an intuitive picture, behind a process has often proven to be of considerable importance for the progress in intense-field physics in the past. Moreover, IMST may also be used to construct simple mathematical models of a process, since it can suggest appropriate places for the introduction of 'physical' hypotheses in the theory. This can be particularly useful for gaining insights into complex situations that may be practically *inaccessible* to an *ab initio* analysis.

In this topical review, in accordance with the spirit of this series of reviews, we shall restrict ourselves to the topic of intense-field many-body S-matrix theory. We shall begin with an outline of the derivation of the IMST series, point out its relation to the usual 'prior' and 'post' series and show its special structural flexibilities for applications to concrete problems (specially for problems with more than one active electron). Next, we shall briefly discuss the results of applications to phenomena that are dominated by a single active electron of an atom in an intense field, and briefly consider its relativistic extension. The interested reader

might note that related S-matrix calculations of single electron processes have been reviewed recently in e.g. [47, 48, 24, 142], earlier relativistic S-matrix calculations have been reviewed some time ago [183]. Next, we shall discuss a consistent S-matrix formulation of the problem of high harmonic generation (HHG), discuss the relation between the single-atom and many-atom HHG signals and their coherent nature and related properties. Finally, we shall focus on the application of IMST to more complex processes such as double (and multiple) ionization of two- and many-electron atoms, and ionization of diatomic and polyatomic molecules in intense fields. We shall end with a summary and an outlook.

3. Intense-field many-body S-matrix theory

3.1. Derivation

The Schrödinger equation of an n-electron system in an electromagnetic field is given in dipole approximation and velocity gauge by (Hartree atomic units, i.e. $\hbar = e = m_e = 1$, are used throughout):

$$i \frac{\partial}{\partial t} \Psi(\mathbf{r}_1, \ldots, \mathbf{r}_n; t) = \left(\frac{1}{2} \sum_{i=1}^{n} \left(\hat{\mathbf{p}}_i - \frac{\mathbf{A}(t)}{c} \right)^2 + V_C(\mathbf{r}_1, \ldots, \mathbf{r}_n) \right) \Psi(\mathbf{r}_1, \ldots, \mathbf{r}_n; t). \tag{1}$$

It includes the laser interaction with all the electrons, where $\mathbf{A}(t)$ is the vector potential of the field, and the long-ranged Coulomb interactions, V_C, among all the charged particles (electrons and nuclei) in an atom or a molecule. The usual perturbation theory for multiphoton ionization is based on the expansion of the wavefunction in terms of the vector potential of the field which, as indicated already, is known to break down for field strengths between 10^{12} W cm^{-2} and 10^{13} W cm^{-2}. For higher intensities, alternative schemes of expansion have had to be developed, in which the electron–photon interaction can be accounted for directly to all orders, already at the level of the leading terms. One such possibility is given by the use of Volkov wavefunction of a free electron in an intense laser field [206], or more specifically its non-relativistic version in dipole approximation (e.g. [55], p 10) as well as the associated Volkov Green's function.

The IMST, as introduced by Faisal and Becker [65, 16], is a systematic reformulation of the usual S-matrix series of the transition amplitude, which is based on *three* different partitions of the total Hamiltonian. At first, the Schrödinger equation of the interacting system (e.g. laser + many-body system) is rewritten as a time-dependent generalization of the Lippmann–Schwinger equation satisfying the initial condition (e.g. the atom or molecule in the ground state at an initial time t_i). Then the usual partition of the total Hamiltonian of the system

$$H(t) = H_i^0(t) + V_i(t), \tag{2}$$

is used, where $H_i^0(t)$ in the 'unperturbed target' Hamiltonian and $V_i(t)$ is the interaction with the external laser field (for the sake of simplicity we drop explicit indications of the coordinates). Then the Schrödinger equation of the total system is rewritten as an integral equation

$$|\Psi(t)\rangle = |\phi_i(t)\rangle + \int_{t_i}^{t_f} dt_1 G(t, t_1) V_i(t_1) |\phi_i(t_1)\rangle \tag{3}$$

with $t_f > t$ and $G(t, t')$ is the total Green's function (or propagator), defined by

$$\left[i \frac{\partial}{\partial t} - H(t) \right] G(t, t') = \delta(t - t') \tag{4}$$

and, $\phi_i(t)$ is a solution of the Schrödinger equation of the unperturbed Hamiltonian $H_i^0(t)$,

$$\left[i \frac{\partial}{\partial t} - H_i^0(t) \right] |\phi_i(t)\rangle = 0. \tag{5}$$

Next, the final-state partition of the total Hamiltonian

$$H(t) = H_f^0(t) + V_f(t) \tag{6}$$

is introduced, where $H_f^0(t)$ is the final-state reference Hamiltonian and $V_f(t)$ is the final-state interaction. The total Green's function is then expanded in terms of the final-state Green's function, $G_f^0(t, t')$, in the form

$$G(t, t') = G_f^0(t, t') + \int_{t_i}^{t_f} dt_1 G_f^0(t, t_1) V_f(t_1) G(t_1, t'), \tag{7}$$

where $G_f^0(t, t')$ satisfies

$$\left[i \frac{\partial}{\partial t} - H_f^0(t) \right] G_f^0(t, t') = \delta(t - t'). \tag{8}$$

Expansion (7) is inserted in the expression for the total wavefunction $|\Psi(t)\rangle$, equation (3), to get

$$|\Psi(t)\rangle = |\phi_i(t)\rangle + \int_{t_i}^{t_f} dt_1 G_f^0(t, t_1) V_i(t_1) |\phi_i(t_1)\rangle$$
$$+ \int_{t_i}^{t_f} \int_{t_i}^{t_f} dt_2 \, dt_1 G_f^0(t, t_2) V_f(t_2) G(t_2, t_1) V_i(t_1) |\phi_i(t_1)\rangle. \tag{9}$$

We note that this is a *closed* form representation of the wavefunction of the system. The above form of the wavefunction automatically satisfies the initial-state condition $\Psi(t = t_i) = \phi_i(t_i)$, where $\phi_i(t) = \exp(-i E_i t)\phi_i$ is one or a linear combination of the eigenstates, $\{\phi_j\}$, with energies E_j, of the unperturbed Hamiltonian of the target Hamiltonian or $H_i \phi_j = E_j \phi_j$. In the above form, the total wavefunction is well arranged for computing the probability amplitude for a transition to a given final state of *any* final reference Hamiltonian. This is because the projection onto any state of the final reference Hamiltonian, $|\phi_f(t)\rangle$, extracts only *one* term (or a linear combination there of) from the reference Green's function G_f^0 (given in the proper state representation). Thus, the transition amplitude typically becomes

$$(S - 1)_{fi}(t_f, t_i) = -i \left[\int_{t_i}^{t_f} dt_1 \langle \phi_f(t_1) | V_i(t_1) | \phi_i(t_1) \rangle \right.$$
$$\left. + \int_{t_i}^{t_f} \int_{t_i}^{t_f} dt_2 \, dt_1 \langle \phi_f(t_2) | V_f(t_2) G(t_2, t_1) V_i(t_1) | \phi_i(t_1) \rangle \right]. \tag{10}$$

This is an exact *master equation* for the S-matrix, where the orthogonal projections for the initial and the final states are carried out *independently* of equal or unequal reference Hamiltonians. Such a formulation is especially useful for problems, in which the final-state reference Hamiltonian is *not* identical to the initial-state reference Hamiltonian.

Another important feature of equation (10) is that the total Green's function appears *between* the initial and the final interactions. This is unlike the appearance of either the initial *or* the final-state interaction as in the usual 'prior' form (see the usual Dirac perturbation series or the Dyson series of the evolution operator in quantum mechanical text books) and the 'post' form (see e.g. [96, 181]). The structural flexibility of IMST permits the introduction of any *virtual* intermediate fragments-propagator of interest, already in the leading terms of the IMST, independently of the initial and the final reference states. In contrast, it should be noted that inclusion of the effects of such intermediate fragment or 'doorway' states (which belong

neither to the initial nor to the final reference Hamiltonians) within the usual 'prior' or 'post' expansion may only be attempted, if at all, by summing those series to very high orders, if not to infinite orders.

To illustrate this distinct character of the IMST, we explicitly introduce the third (intermediate) partition of the total Hamiltonian:

$$H(t) = H_0(t) + V_0(t),\tag{11}$$

which corresponds to the intermediate (virtual) Hamiltonian $H_0(t)$. The corresponding propagator $G_0(t, t')$ is then used to expand $G(t, t')$ as

$$G(t, t') = G_0(t, t') + \int_{t_i}^{t_f} dt_1 G_0(t, t_1) V_0(t_1) G_0(t_1, t') + \cdots.\tag{12}$$

Substitution of equation (12) into equation (10) gives the transition amplitude as the desired S-matrix series (IMST):

$$(S - 1)_{fi}(t_f, t_i) = \sum_{j=1}^{\infty} S_{fi}^{(j)}(t_f, t_i)\tag{13}$$

with

$$S_{fi}^{(1)}(t_f, t_i) = -\mathrm{i} \int_{t_i}^{t_f} dt_1 \langle \phi_f(t_1) | V_i(t_1) | \phi_i(t_1) \rangle\tag{14}$$

$$S_{fi}^{(2)}(t_f, t_i) = -\mathrm{i} \int_{t_i}^{t_f} \int_{t_i}^{t_f} dt_2\, dt_1 \langle \phi_f(t_2) | V_f(t_2) G_0(t_2, t_1) V_i(t_1) | \phi_i(t_1) \rangle\tag{15}$$

$$S_{fi}^{(3)}(t_f, t_i) = -\mathrm{i} \int_{t_i}^{t_f} \int_{t_i}^{t_f} \int_{t_i}^{t_f} dt_3\, dt_2\, dt_1 \langle \phi_f(t_3) | V_f(t_3)$$
$$\times\, G_0(t_3, t_2) V_0(t_2) G_0(t_2, t_1) V_i(t_1) | \phi_i(t_1) \rangle\tag{16}$$

$$\cdots = \cdots.$$

We may point out that the presence of the Green's functions *automatically* takes care of both the time ordering as well as the range of the intermediate time integrations, and hence they all have a convenient common range, t_i to t_f, above.

3.2. Comparison with other S-matrix series

It is interesting to see how one can re-obtain the usual 'prior' and 'post' versions of the S-matrix expansions as restricted *special* cases of IMST. Thus, the IMST series reduces immediately to the 'prior' form of the S-matrix series for the restricted choice,

$$G_0(t, t') = G_f^0(t, t') \qquad \text{and} \qquad V_0(t) = V_f(t),\tag{17}$$

where the same reference Hamiltonian is used in the initial and the intermediate partitions. Thus, in this case we get

$$(S - 1)_{fi}(t_f, t_i) = -\mathrm{i} \int_{t_i}^{t_f} dt_1 \langle \phi_f(t_1) | V_i(t_1) | \phi_i(t_1) \rangle$$
$$-\, \mathrm{i} \int_{t_i}^{t_f} \int_{t_i}^{t_f} dt_2\, dt_1 \langle \phi_f(t_2) | V_f(t_2) G_f^0(t_2, t_1) V_i(t_1) | \phi_i(t_1) \rangle$$
$$-\, \mathrm{i} \int_{t_i}^{t_f} \int_{t_i}^{t_f} \int_{t_i}^{t_f} dt_3\, dt_2\, dt_1 \langle \phi_f(t_3) | V_f(t_3)$$
$$\times\, G_f^0(t_3, t_2) V_f(t_2) G_f^0(t_2, t_1) V_i(t_1) | \phi_i(t_1) \rangle - \mathrm{i} \ldots$$
$$= \int_{t_i}^{t_f} dt_1 \langle \Psi_f(t_1) | V_i(t_1) | \phi_i(t_1) \rangle,\tag{18}$$

where $|\Psi_f(t)\rangle$ is the full wavefunction satisfying the final-state condition. The last line follows on keeping $|V_i(t)|\phi_i(t)\rangle$ on the extreme right fixed in each term, collecting the rest (term by term) together and recognising that they add up to $|\Psi_f(t)\rangle$, the total wavefunction satisfying the *final*-state condition.

We may note further that in the same way one would get the standard perturbation series (i.e. Dirac's time-dependent perturbation theory) with a single partition of the Hamiltonian (as used for LOPT in the low intensity regime) in the special case in which all the reference Hamiltonians, and interactions, are restricted to be the same:

$$G_0(t, t') = G_i^0(t, t') = G_i^0(t, t) \qquad \text{and} \qquad V_0(t) = V_i(t) = V_f(t). \quad (19)$$

The 'post' form of the series can be obtained from IMST in the special case [68],

$$G_0(t, t') = G_i^0(t, t') \qquad \text{and} \qquad V_0(t) = V_i(t). \quad (20)$$

Substituting them in equation (13), and adding and subtracting a term,

$$-\mathrm{i} \int_{t_i}^{t_f} \mathrm{d}t_1 \langle \phi_f(t_1)|V_f(t_1)|\phi_i(t_1)\rangle, \quad (21)$$

we may rewrite the equation as,

$$
\begin{aligned}
(S-1)_{fi}(t_f, t_i) &= \Delta(t_i, t_f) - \mathrm{i} \int_{t_i}^{t_f} \mathrm{d}t_1 \langle \phi_f(t_1)|V_f(t_1)|\phi_i(t_1)\rangle \\
&\quad - \mathrm{i} \int_{t_i}^{t_f} \int_{t_i}^{t_f} \mathrm{d}t_2\, \mathrm{d}t_1 \langle \phi_f(t_2)|V_f(t_2)G_i^0(t_2, t_1)V_i(t_1)|\phi_i(t_1)\rangle \\
&\quad - \mathrm{i} \int_{t_i}^{t_f} \int_{t_i}^{t_f} \int_{t_i}^{t_f} \mathrm{d}t_3\, \mathrm{d}t_2\, \mathrm{d}t_1 \langle \phi_f(t_3)|V_f(t_3) \\
&\quad \times G_i^0(t_3, t_2)V_i(t_2)G_i^0(t_2, t_1)V_i(t_1)|\phi_i(t_1)\rangle - \mathrm{i}\ldots \\
&= \Delta(t_i, t_f) - \mathrm{i} \int_{t_i}^{t_f} \mathrm{d}t_1 \langle \phi_f(t_1)|V_f(t_1)|\Psi_i(t_1)\rangle \\
&= -\mathrm{i} \int_{t_i}^{t_f} \mathrm{d}t_1 \langle \phi_f(t_1)|V_f(t_1)|\Psi_i(t_1)\rangle \quad (22)
\end{aligned}
$$

since, the difference integral

$$
\begin{aligned}
\Delta(t_i, t_f) &\equiv -\mathrm{i} \int_{t_i}^{t_f} \mathrm{d}t_1 \langle \phi_f(t_1)|V_i(t_1) - V_f(t_1)|\phi_i(t_1)\rangle \\
&= -\mathrm{i} \langle \phi_f(t_1)|\phi_i(t_1)\rangle\big|_{t_1=t_i\to-\infty}^{t_1=t_f\to\infty} = 0 \qquad (\phi_f \neq \phi_i) \quad (23)
\end{aligned}
$$

and does not contribute to the transition *rate*. Equation (23) can be readily verified using equations (2) and (6) along with the Schrödinger equations for the initial and the final reference Hamiltonians followed by a partial integration ([68], footnote 11)[4]. In the last line of equation (22) $|\Psi_i(t)\rangle$ is the total wavefunction of the system satisfying the *initial*-state condition; it can be seen to arise from the series in equation (22) (without $\Delta(t_i, t_f)$) on taking the common factor $\langle \phi_f(t)|V_f(t)|$ in each term outside, and collecting the rest (term by term) together and recognising that they add up to the total wavefunction satisfying the initial-state condition. Equation (22) is nothing but the 'post' form of the usual S-matrix amplitude.

---

[4] We may point out that in the case of a finite or short time interval $(t_f - t_i)$, the overlap in equation (23) can be readily evaluated and added to the rest of the amplitude and the probability of the process determined directly by modulo squaring the amplitude.

The above demonstrations make it clear that the IMST contains all the usual forms of S-matrix expansions ('prior', 'Dirac' and 'post') as special cases and that they can be generated by merely *restricting* the IMST in different ways, if desired. More importantly, a term-by-term comparison of the IMST series, equations (13)–(16), with the prior and post forms, equations (18) and (22), makes it clear that the IMST differs *qualitatively* from the latter S-matrix expansions, beginning from the *second* term onwards. Combining with the flexibility of IMST, this opens up the possibility of accounting for qualitatively different reaction processes already within the *leading* terms of the series. This flexibility suggests considerable potential usefulness of the IMST for different many-body *reaction* problems in strong-field physics and beyond, e.g. for charge–exchange reactions, for chemical reactions and for rearrangement processes in general which invariably involve unequal reference Hamiltonians in the input and the output channels and are often governed by intermediate reference Hamiltonians related to the so-called 'transition states', the 'door-way' states or the states of 'virtual fragments' which crucially mediate a reaction process. Finally we should point out that, if and when needed, more than three partitions of the total Hamiltonian can be introduced by additional intermediate partitions and associated Green's functions as in equations (11) and (12).

4. Single-active-electron processes in atoms

In this section, we consider applications of the S-matrix theory to atomic single-active-electron processes in intense laser fields. We present explicit expressions for the lowest order terms of the IMST series for laser-induced *ionization* and also introduce the corresponding diagrammatic representation of the terms. Next, the *tunnel* ionization limit of the resulting well-known KFR rate formula is shown to clarify the transition from the 'photon picture' to the 'field-ionization' picture in intense fields. Results of the IMST for the analysis of the experimental total ion *yields* versus the laser intensity and of the energy spectra of the electrons are then discussed. We also discuss the S-matrix formulation of the quantum HHG *amplitude* and point out its equivalence with the alternative formulations in terms of the expectation value of the semi-classical currents. In this context we discuss some of the most important general properties of the HHG radiation, its relation with ATI and the role of the single-atom emission spectrum to the many-atom signal, with special reference to the conditions for the coherent amplification in the latter case, and of 'hyper-Raman' emission.

4.1. Ionization in intense fields

We note first that the basic laser-atom interaction consists of a sum of individual *single-particle* interactions of light with the atomic electrons (cf equation (1)). This circumstance is responsible for many optical phenomena that can be reasonably accounted for by the behaviour of an active (usually valence) electron in the laser field. It also allows one to use approximately a single-active-electron (or SAE) model for the problem of electron emission from an atom (or capture of the free electron by the ion) in intense fields.

In the SAE approximation [119], the active electron is assumed to be independently moving in the effective potential formed by the ion core and the rest of the electrons. The Schrödinger equation of the system, equation (1), then reduces to

$$i\frac{\partial}{\partial t}\Psi(\boldsymbol{r};t) = \left(\frac{\hat{\boldsymbol{p}}^2}{2} + V_L(t) + V_a(\boldsymbol{r})\right)\Psi(\boldsymbol{r};t), \tag{24}$$

where

$$V_L(t) = -\frac{\hat{\pmb{p}} \cdot \pmb{A}(t)}{c} + \frac{A^2(t)}{2c^2} \tag{25}$$

is the laser-electron interaction potential in the minimal coupling or velocity gauge, and V_a is the effective atomic potential. Both of these two interactions are of comparable relevance for the dynamics of the total system in intense fields. Thus, to obtain the dominant contribution to the transition probability for any single-active-electron process in intense fields, it is sufficient to use only two splittings of the total Hamiltonian in the S-matrix expansion. For example, for the dominant contribution to the ionization we use the following partitions:

$$H_i^0 = \frac{\hat{\pmb{p}}^2}{2} + V_a(\pmb{r}) \qquad \text{with} \quad V_i(t) = V_L(t), \tag{26}$$

which easily allows one to fulfil the initial condition of the unperturbed (one-electron) atom in its bound state, $\phi_i(\pmb{r}, t)$, which is an eigenstate of the atomic Hamiltonian H_i^0. For the final and intermediate states we may use here the same partition,

$$H_f^0(t) = H_0(t) = \frac{\hat{\pmb{p}}^2}{2} + V_L(t) \qquad \text{with} \quad V_f = V_0 = V_a(\pmb{r}). \tag{27}$$

This partition accounts for the dominant intense-field interaction both in the intermediate and the final states of the system. The first two terms of the resulting expansion of the S-matrix element for ionization, in which an electron is emitted in the field with an asymptotic momentum $\pmb{k}_a$, are then given by equations (14) and (15):

$$S_{fi}^{(1)}(t_f, t_i) = -\mathrm{i} \int_{t_i}^{t_f} \mathrm{d}t_1 \langle \phi_{\pmb{k}_a}^V(\pmb{r}; t_1) | V_L(t_1) | \phi_i(\pmb{r}; t_1) \rangle \tag{28}$$

$$S_{fi}^{(2)}(t_f, t_i) = -\mathrm{i} \int_{t_i}^{t_f} \int_{t_i}^{t_2} \mathrm{d}t_2\, \mathrm{d}t_1 \int \mathrm{d}\pmb{k} \langle \phi_{\pmb{k}_a}^V(\pmb{r}; t_2) | V_C(\pmb{r}) | \phi_{\pmb{k}}^V(\pmb{r}; t_2) \rangle$$
$$\times \langle \phi_{\pmb{k}}^V(\pmb{r}; t_1) | V_L(t_1) | \phi_i(\pmb{r}; t_1) \rangle, \tag{29}$$

where the angular brackets denote here and below, integrations with respect to the coordinates, and (in this notation) the well-known Volkov wavefunction ([206] or, [55]) is denoted by,

$$\phi_{\pmb{k}}^V(\pmb{r}; t) = \exp\left(-\mathrm{i} \int_{-\infty}^{t} \mathrm{d}t'\, E_k(t')\, \mathrm{d}t'\right) \phi_{\pmb{k}}(\pmb{r}), \tag{30}$$

where,

$$E_k(t) = \frac{1}{2} \left(\pmb{k} - \frac{\pmb{A}(t')}{c} \right)^2. \tag{31}$$

In the above we have used the Volkov Green's function, given explicitly by

$$G_0(t, t') = -\mathrm{i}\theta(t - t') \int \mathrm{d}\pmb{k} |\phi_{\pmb{k}}(\pmb{r})\rangle \exp\left(-\mathrm{i} \int_{t'}^{t} E_k(t'')\, \mathrm{d}t''\right) \langle \phi_{\pmb{k}}(\pmb{r})|, \tag{32}$$

where $\phi_{\pmb{k}}(\pmb{r}) = \exp(\mathrm{i}\pmb{k} \cdot \pmb{r})/(2\pi)^{3/2}$ are the usual plane waves.

As usual, it is convenient and useful to obtain an intuitive picture of the 'mechanism' involved by representing the terms of the ionization amplitudes by Feynman-like diagrams. For a single-active-electron process, the non-trivial first and second leading terms of the S-matrix series give rise to the two diagrams shown in figures 1(a) and (b). In these diagrams, as well as in all other diagrams discussed below, it is helpful to assume that time flows from the bottom upwards; the straight lines stand for the evolution of the state of the active electron(s); the notation '—x' stands for the interaction with the laser field, and the horizontal line '—'

(a)   (b)
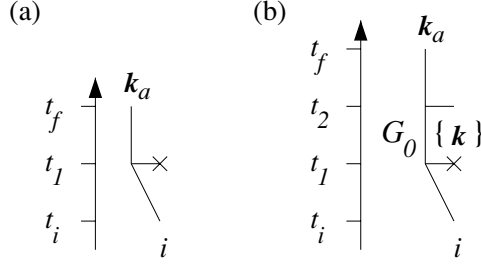
Figure 1. Diagrams generated by the IMST for ionization of an atom (molecule): (a) first-order term, (b) second-order term.

stands for the Coulomb interaction of the electron with the core. G_0 is the propagator of the electron in the field which for the present case is defined by a complete set of Volkov states in the intermediate states; a 'nick' on the electron line(s) denotes the change of the state of the electron due to a change in the reference Hamiltonian (or propagator) in the amplitude[5].

Thus, according to the diagram in figure 1(a), the electron evolves from an initial time, $t = t_i$, in the bound state of the atom and interacts with the laser field at $t = t_1$, is ejected from the atom in the presence of the laser field and finally observed at the detector at a time $t_f \rightarrow \infty$, with an asymptotic final momentum $\boldsymbol{k}_a$, when the field is assumed to be switched off adiabatically. This lowest order contribution to ionization is often referred to as 'direct ionization' (cf, e.g. [24]), since the electron leaves the atom without further interaction with the residual ion core.

In the next order term (figure 1(b)) the electron propagates during the interval of time $\Delta t = t_2 - t_1$ in the laser field, after its initial interaction with the field at $t = t_1$, and then gets scattered by the Coulomb interaction with the residual ion core at $t = t_2$ and emerges with the asymptotic final momentum $\boldsymbol{k}_a$ and ceases to interact with the field (as it switches off adiabatically). The second-order contribution is often referred to as 'rescattering', since it involves a scattering of the electron, when it is in the (intermediate) Volkov state, with the ion core. This mechanism was envisaged classically and semi-classically by Corkum and others [190, 38].

4.2. Ionization rate and KFR formula

In the expansion of the S-matrix for strong-field ionization, one basically makes use of the Volkov wavefunction of a free electron in an electromagnetic field, equation (30), or the associated Green's function, equation (32), to take account of the laser interaction of a single electron to all orders. Thus using the Volkov wavefunction for the final state, in the first term of equation (13), one can easily obtain the ionization rate for a general elliptically polarized vector potential,

$$\boldsymbol{A}(t) = A_0 \left(\boldsymbol{\epsilon}_1 \cos \frac{\xi}{2} \cos(\omega t) - \boldsymbol{\epsilon}_2 \sin \frac{\xi}{2} \sin(\omega t) \right), \tag{33}$$

where the propagation is chosen along the 3-axis and $\boldsymbol{\epsilon}$ are orthogonal unit polarization vectors. ξ is the ellipticity of the field and ranges between $[0, \pm\pi/2]$ with $\xi = 0$ for linear polarization and $\xi = \pi/2$ for circular polarization ($\pm$ correspond to right or left helicity).

---

[5] Note that the associated state of the core or the nucleus can also be represented by additional lines etc, but they do not require to be drawn explicitly for reproducing the amplitude from the diagrams given here; we have therefore adopted a simpler convention of showing explicitly only the essential states of the electron motions for the process.

It is useful first to Fourier expand the Volkov wavefunction using the Jacobi–Anger formula,

$$\exp(iz \sin\theta) = \sum_{n=-\infty}^{\infty} J_n(z) \exp(in\theta), \tag{34}$$

where $J_n(z)$ is the ordinary Bessel function:

$$\phi_k^V(r; t) = \phi_k(r) \sum_{N=-\infty}^{\infty} \exp\left(-i\left[\frac{k^2}{2} + U_p - N\omega\right]t\right) J_N(a_k; b; \chi). \tag{35}$$

Here

$$J_N(a_k; b; \chi) = \sum_{m=-\infty}^{\infty} J_{N+2m}(a_k) J_m(b) \exp[i(N + 2m)\chi] \tag{36}$$

is the generalized Bessel function of *three* arguments (cf [8, 181, 55]) with

$$a_k = \alpha_0 \sqrt{\left(\epsilon_1 \cdot k \cos\frac{\xi}{2}\right)^2 + \left(\epsilon_2 \cdot k \sin\frac{\xi}{2}\right)^2}, \tag{37}$$

$$b = \frac{U_p}{2\omega} \cos\xi, \tag{38}$$

$$\chi = \arctan\left(\frac{\epsilon_2 \cdot k}{\epsilon_1 \cdot k} \tan\frac{\xi}{2}\right), \tag{39}$$

$\alpha_0 = \sqrt{I}/\omega^2$ is the quiver radius and $U_p = I/4\omega^2$ is the ponderomotive (or quiver) energy[6]. Using

$$\left(-\frac{\hat{p} \cdot A(t)}{c} + \frac{A^2(t)}{2c^2}\right) |\phi_k^V(r; t)\rangle = \left(i\frac{\partial}{\partial t} - k^2/2\right) |\phi_k^V(r; t)\rangle \tag{40}$$

and equation (35), in the first-order term of the S-matrix expansion, equation (28), we get

$$S_{fi}^{(1)}(t_f, t_i) = -i \sum_{N=-\infty}^{\infty} \int_{t_i}^{t} dt_1 \exp\left(i\left(\frac{k^2}{2} + U_p + I_p - N\omega\right)t_1\right)$$
$$\times (U_p - N\omega) J_N(a_k, b, \chi)\langle\phi_k(r)|\phi_i(r)\rangle, \tag{41}$$

where I_p is the ionization potential of the target atom in the ground state ϕ_i. Assuming long pulses (durations much longer than a laser period $T = 2\pi/\omega$), letting $t_i \to -\infty$ and $t = t_f \to \infty$, and evaluating the time integration analytically, we have the ionization amplitude,

$$S_{fi}^{(1)}(t_f, t_i) = -2\pi i \sum_{N=-\infty}^{\infty} \delta\left(\frac{k^2}{2} + U_p + I_p - N\omega\right)(U_p - N\omega) J_N(a_k, b, \chi)\langle\phi_k(r)|\phi_i(r)\rangle. \tag{42}$$

On modulo squaring the amplitude for the N-photon transition and using a convenient representation of the square of the delta function ([55], p 48),

$$\delta^2(x) = \delta(x)\delta(x) = \lim_{\tau\to\infty} \frac{\tau}{2\pi}\delta(x), \tag{43}$$

---

[6] The ponderomotive (or quiver) energy $U_p = I/4\omega^2$ is the cycle-averaged kinetic energy of a free electron in the laser field of intensity I and frequency ω.

and dividing the resulting probability by the (long) interaction time τ, one obtains the well-known KFR *rate* formula [100, 53, 181] for the probability per unit time of direct electron-ejection (per target electron) in which the electron is emitted, by absorption of N photons, in a cone-angle $\mathrm{d}\hat{k}_N$:

$$\frac{W_{\mathrm{KFR}}^{(N)}}{\mathrm{d}\hat{k}_N} = 2\pi k_N (U_p - N\omega)^2 J_N^2 (a_{k_N}, b, \chi) |\langle \phi_{k_N}(r) | \phi_i(r) \rangle|^2, \tag{44}$$

where $k_N^2/2 = N\omega - (U_p + I_p)$ is the kinetic energy of the electron. On integration over the emission angles $\hat{k}_N$, and summation over the absorbed photons N, one obtains the total ionization rate:

$$\Gamma_{\mathrm{KFR}}^+ = 2\pi \sum_{N=N_0}^{\infty} k_N (U_p - N\omega)^2 \int \mathrm{d}\hat{k}_N J_N^2 (a_{k_N}, b, \chi) |\langle \phi_{k_N}(r) | \phi_i(r) \rangle|^2, \tag{45}$$

where $N_0 = [(I_p + U_p)/\omega]_{\mathrm{int}} + 1$ is the minimum number of photons needed to be absorbed for the emission of an electron. The total rate obviously consists of the sum of probabilities for the rate of individual N-photon ATI absorption above the field-shifted ionization threshold $(I_p + U_p)$. They are determined by the energy conserving delta functions in equation (42).

The physical structure of the N-photon ionization rate in the KFR formula, equation (45), can be easily understood in terms of its dependence on the four factors that appear there. Thus, the first factor k_N arises from the density of continuum states at the N-photon ATI peak at the momentum k_N, the second factor $(N\omega - U_p)^2$ is associated with the energy, $(N\omega - U_p)$, transferred from the field to the atom, the third factor J_N^2 is the probability of a Volkov electron to virtually absorb N photons (at the momentum k_N) and the last factor $|\langle \phi_{k_N} | \phi_i \rangle|^2$ is the probability of finding the real momentum k_N, in the bound state of the atom. Note that it is the presence of the bound-state momentum distribution that renders the virtual absorption probability of a Volkov electron to be real in the continuum state of the atom. The necessary energy conservation is provided by the energy of the laser photons but the necessary momentum conservation is supplied by the bound-state momentum distribution. The last factor can also be viewed upon as due to the transfer of the necessary momentum by collision with the potential centre (in first Born approximation) that binds the atom in its initial state. We may add that the momentum transferred by the (optical or longer wavelength) laser photons is too small, even when not assumed to be zero as in the dipole approximation, to allow for the momentum-transfer necessary for the ionization transition.

4.3. Tunnel ionization limit

It is worthwhile to note that the KFR formula, equation (45), which explicitly shows the probability for absorption for discrete *photons* also contains the usual tunneling formula based on the 'field-ionization' picture which does not seem to depend on the photon picture at all. In fact the essential tunnel-like probability can arise as a limiting case of the photon picture, e.g. as a special case of the KFR formula in the limit $\gamma \equiv \sqrt{I_p/(2U_p)} = \omega k_B/F \ll 1$, where $k_B = \sqrt{2I_p}$ and $F^2 = I$. This limit has been originally considered by Keldysh [100] who also introduced the now well-known γ parameter given above. That the KFR rate formula contains the tunnel formula can be shown by evaluating the generalized Bessel function in the above limit using the integral representation,

$$J_n(a, b) = \frac{1}{2\pi} \int_0^{2\pi} \mathrm{d}\phi \exp(\mathrm{i}n\phi - \mathrm{i}a\sin\phi + \mathrm{i}b\sin 2\phi). \tag{46}$$

For large exponents we may use the stationary-phase method to evaluate it and take the small γ-limit as done by Keldysh and others (e.g. [100, 167]). For example, in the case of an electron

bound by a short range s-wave potential, the Fourier transform of the ground state is of the form $\tilde{\phi}_i(\mathbf{k}) = \langle \phi_{\mathbf{k}}(\mathbf{r}) | \phi_i(\mathbf{r}) \rangle = B_0 \frac{\sqrt{4\pi}}{k^2 + k_B^2}$ where B_0 is a suitable normalization constant. The result of the stationary-phase integration reduces equation (45) to,

$$\Gamma_{\text{quasi-stat.}} = 2\pi \int d\mathbf{k} \frac{c_0}{\pi k_B^2} B_0^2 \exp\left[-\left(c_1 + c_2 \frac{k_\parallel^2}{k_B^2} + c_3 \frac{k_\perp^2}{k_B^2} \right) \right]$$

$$\times \left(1 + (-1)^n \cos(2k_B k_\parallel c_4) \right) \left| \frac{(k_B^2 + k^2)}{2} \phi_i(\hat{\mathbf{k}}) \right|^2, \tag{47}$$

with $k_\parallel$ and $k_\perp$ are the momentum components parallel and perpendicular to the field direction. In equation (47) the sum over the N is carried out approximately by an integration over $\frac{1}{\omega} d(N\omega)$ which can be performed effortlessly with the help of the delta function (cf equation (42)). Note that it is at this stage that the explicit 'photon picture' goes over, as an *approximation*, to the 'field-ionization' picture. Clearly therefore the two pictures are not in conflict with each other but only that the latter is convenient for practical purposes in the small γ-limit. In this limit the coefficients c_i, $i = 0, \dots, 4$ are found to be,

$$c_0 = \frac{\gamma}{1 + \gamma^2} \approx \gamma \qquad c_1 = \frac{k_B^2}{\omega} \frac{2\gamma}{3} = \frac{2F_B}{3F} \qquad c_2 = \frac{k_B^2}{\omega} \frac{\gamma^3}{3} = \frac{F_B}{3F} \gamma^2$$

$$c_3 = \frac{k_B^2}{\omega} \gamma = \frac{F_B}{F} \qquad c_4 = \frac{\sqrt{1 + \gamma^2}}{\gamma \omega} \approx O(\omega^{-2}),$$

where the characteristic atomic field strength F_B is defined as $F_B \equiv k_B^3$.

The argument of the cosine term in equation (47) is clearly of the order of $O(\omega^{-2})$ and, hence, oscillates rapidly as $\omega \to 0$ and becomes negligible in the tunnel limit (but only in the mean). Hence, in principle (and contrary to the usual assumption) it can give rise to a quantum interference effect even in the tunneling regime. If one however neglects the interference term as usual, then introducing the cylindrical coordinates, and using the integrals, $\int_0^\infty dk_\perp k_\perp \exp\left(-ak_\perp^2\right) = \frac{1}{2a}$, and $\int_{-\infty}^\infty dk_\parallel \exp\left(-ak_\parallel^2\right) = \sqrt{\frac{\pi}{a}}$, and simplifying, one obtains for the electron-emission rate (in the quasi-static tunneling limit) from the KFR rate formula, equation (45), (for short range potentials):

$$\Gamma_{\text{quasi-stat.}} = \frac{B_0^2 k_B}{4} \frac{F}{F_B} \sqrt{\frac{3F}{\pi F_B}} \exp\left(-\frac{2F_B}{3F} \right). \tag{48}$$

Note that it gives the usual linear field dependence in the pre-exponential factor of the tunnel formula for a short range potential *and* an extra factor $\sqrt{\frac{3F}{\pi F_B}}$. This factor is a consequence of the fundamental difference between a long sinusoidal laser field that changes sign every half a period (even in the slowly varying quasistatic limit) compared to the case of a purely static field that has a fixed sign throughout. This pre-exponential factor is a distinguishing sign of 'optical' tunnel ionization as opposed to the tunnel ionization in a static field. It is interesting to note that the extra intensity-dependent factor can also be obtained heuristically by replacing the static field strength F in the usual field-emission formula by $F \cos \omega t$ *and* averaging with respect to the phase ωt of the oscillation over a period as shown by Perelomov *et al* [167]. We may further note that besides this extra 'oscillation factor' there is a difference between the F dependence of the forefactor in equation (48) for static field electron detachment [42] and for static field *ionization* [197]. The field dependence for ionization can be recovered by a simple correction of the KFR formula that arises from the long range Coulomb tail and is briefly discussed in the next subsection. Here we may make use of the result and simply multiply

the Coulomb correction factor $C^2 = \left(\frac{F_B}{F}\right)^{2Z/k_B}$ (see equation (51)) with equation (48). This gives the quasi-static tunnel-ionization rate with appropriate F dependence (for ionization of a s-state atom as assumed in this example):

$$\Gamma_{\text{quasi-stat.}} = \frac{B_0^2 k_B}{4} \sqrt{\frac{3F}{\pi F_B}} \left(\frac{F_B}{F}\right)^{\frac{2Z}{k_B}-1} \exp\left(-\frac{2F_B}{3F}\right). \tag{49}$$

The corresponding tunneling formula for ionization of an atom in a more general state $\{n*, l, m\}$, where $n*$ is the effective principal quantum number, can be obtained in an analogous way (preferably in the length gauge, cf [167]) and is equivalent to the popular ADK-tunnel formula [4]. Note that the corresponding bound-state normalization constant B_l can be determined by analytic continuation of the integer principal quantum number n for hydrogenic atoms to non-integer values $n*$ defined by $I_p = Z^2/(2n*^2)$, where Z is the charge state of the residual ion.

4.4. Ionization yields

As indicated above, originally the plane-wave KFR rate formulae (equation (45)) have been obtained for the problem of electron detachment of negative ions [100, 53, 181], since they do not include the effect of the long-range Coulomb interaction in the final state. Predictions of the plane-wave KFR model if applied to ionization rates (as opposed to detachment rates) underestimate the results of *ab initio* Floquet calculations or *ab initio* numerical simulations for H atom by more than an order of magnitude [195, 15]. Different approaches to replace the Volkov wavefunction by approximate Coulomb–Volkov wavefunctions in the final state have been made (e.g. [90, 99, 91]), but so far they failed to modify the plane-wave KFR model to yield the correct absolute rates. Nikishov and Ritus [153] and Perelemov *et al* [167] in the past, have given estimates in the quasi-static limit of the Coulomb effect in the final state, and more recently Krainov has given a WKB approximation of the Coulomb effect [110]. In order to get a simple Coulomb correction to the plane-wave KFR rate formulae, the latter approximation has been further simplified by evaluating the WKB result at the turning point radius. This led to a simple Coulomb corrected KFR model, proposed by Becker *et al* [15]:

$$\Gamma_{\text{ion.}}^+ = C^2(Z, E_B, F) N_e \Gamma_{\text{KFR}}^+, \tag{50}$$

where

$$C^2(Z, E_B, F) = \left(\frac{2k_B E_B}{F}\right)^{\frac{2Z}{k_B}} = \left(\frac{F_B}{F}\right)^{\frac{2Z}{k_B}}, \tag{51}$$

is the Coulomb correction factor, N_e is the number of equivalent electrons in the ionizing shell of the target, $E_B = k_B^2/2$ and Z is the core charge. Note that the simple correction factor depends both on the field amplitude $F = A_0\omega/c$ and on the charge state, Z, of the residual ion; it reduces to unity for short-ranged potentials with $Z = 0$.

Predictions of the absolute rates from the Coulomb corrected KFR model formula, equations (45) and (50), have been tested by comparing them with the results of (a) *ab initio* Floquet calculations [195] and (b) *ab initio* time-dependent 3D numerical simulations for ionization of the H atom (for both linear and circular polarizations) [15]. The overall agreement has been found to be very satisfactory for intensities in the non-perturbative domain, but below $I \approx 10^{15}$ W cm^{-2} (for ionization of hydrogen). The same bounds on the range of intensities have again been found for H-atom more recently by Reiss [184].

The above formula has then been used to analyse the ionization *yields* measured for the noble gas atoms in a large number of experiments. These provide a good test of the applicability
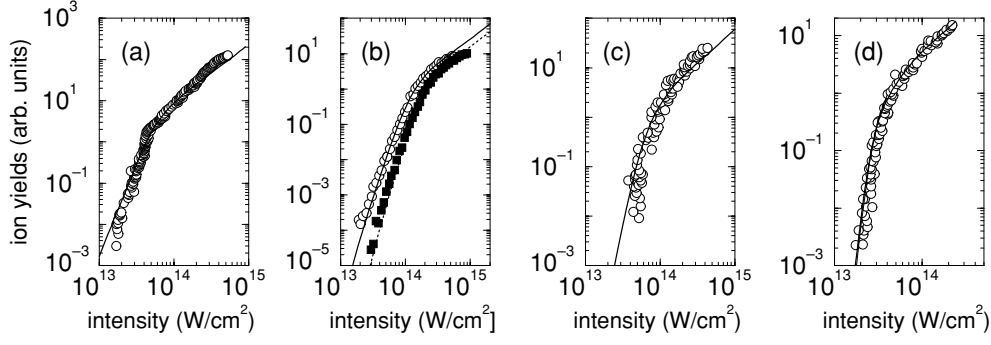
Figure 2. Comparison of the predictions of the Coulomb-corrected KFR model (lines, cf [15]) for the ion yields of a xenon atom with the data sets observed in different experiments, (a) $\lambda = 586$ nm, $\tau = 1$ ps [168, 169], (b) $\lambda = 800$ nm, $\tau = 30$ fs [83], (c) $\lambda = 1053$ nm, $\tau = 1$ ps [3] and (d) $\lambda = 10\,600$ nm, $\tau = 2.6$ ns [210]. Results obtained for a linearly polarized field are given by solid lines (theory) and open circles (experiment), while those for a circularly polarized laser field are marked by dotted lines (theory) and filled squares (experiment).

or otherwise of the Coulomb corrected KFR formula. At present a direct comparison between experiment and theory is not possible at the level of the basic rates of ionization *per* atom. It is necessary therefore to theoretically construct the distributions of ionization yields in the interaction volume that had been measured. Ion yields are determined by combining the fundamental rates, equation (50), with the *rate equations* governing the normalized populations of the neutral atoms, $P_0(r, t)$, and that of the ions, $P(r, t)$,

$$\frac{dP_0(r, t)}{dt} = -\Gamma^+_{ion.}(I(r, t))P_0(r, t) \tag{52}$$

$$\frac{dP(r, t)}{dt} = \Gamma^+_{ion.}(I(r, t))P_0(r, t) \tag{53}$$

at any point in the laser focus, (r, t). The above system of rate equations is solved with the initial conditions, $P_0(r, t = -\infty) = 1$ and $P(r, t = -\infty) = 0$, and the contributions from all points in the focus are added. We may point out here that the respective partial yields for the angular and the energy distributions, if desired, can be obtained in a similar way [94]. We also point out that the rate concept and the use of rate equations are appropriate only when the pulse is not too short and the ionization process remains essentially adiabatic in nature. In the case of ionization of H atoms the onset of adiabaticity has been found, from direct numerical simulations with different pulse lengths, to occur for pulse durations as short as about three cycles of the field [15]. The minimum pulse length for the applicability of the adiabaticity for ionization is therefore about 8 fs for the common Ti:sapphire laser wavelength of 800 nm. We note that this limit appears to coincide with the upper limit at which also the influence of the carrier-envelope phase (i.e. the difference between the phase of the carrier wave with respect to, say, the peak of the pulse envelope) on the emission of ATI electrons becomes significant [166].

The calculated ion yields from the Coulomb corrected KFR formula (equations (45), (50)–(53)) have been tested by Becker *et al* [15] with the experimental data obtained by different authors in 36 individual cases. Together, the experimental data cover a wide wavelength region between $\lambda = 248$ nm and $\lambda = 10\,600$ nm, pulse durations between 2.6 ns and 30 fs, peak intensities between 10^{12} W cm^{-2} and 10^{15} W cm^{-2} as well as cases of both linear and circular polarizations. The calculated yields were found to agree well with all the 36 different cases compared. A typical comparison from this set is exemplified in figure 2 for
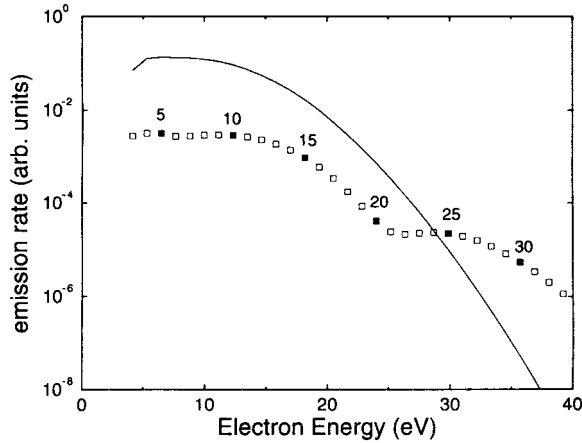
Figure 3. Relative contributions of absolute squares of the first-order 'direct-ionization' (solid line) and the second-order 'rescattering' (squares) amplitudes to the energy spectrum of electrons. Calculations are for a model 'xenon' atom where the long range Coulomb potential is approximated by a zero-range potential; $\omega = 1.17$ eV and $U_p = 3.1$ eV (from [21], reproduced with permission of the authors).

the case of the Xe atom. We may conclude that the good agreement of the predictions of the Coulomb corrected KFR formula with (a) the results of *ab initio* Floquet calculations, (b) 3D numerical simulations for hydrogen atom and finally with (c) available experimental data for ion yields shows the usefulness of this formula for analysing large data sets of ion yields in the low-frequency high-intensity domain, including the frequently employed Ti-sapphire and other intense laser systems.

4.5. Energy spectra of electrons

To determine the energy spectrum of the electrons emitted over a wide range of energy from atoms in intense fields it is necessary to consider the contributions of both the diagrams shown in figures 1(a) and (b), respectively corresponding to the 'direct ionization' and the 'rescattering' mechanisms discussed above. It is interesting to note that not only the sum of the contributions but also the contributions of the two *individual* terms can be identified in the same energy spectrum. This is because the overall shape of the spectrum (in an intense linearly polarized near-infrared laser field) exhibits *two* distinguishable parts: a low-energy part having a rapid fall off near $2U_p$ and a high-energy *plateau* extending up to a *cut-off* energy at about $10U_p$. The low-energy part of the spectrum arises mainly from the first-order diagram figure 1(a), i.e. from the 'direct ionization'. In contrast, the second-order diagram, figure 1(b), is responsible for the electrons that are initially set free by the field and undergo a 'rescattering' with the parent ion, and thus contribute to the high-energy part of the spectrum with a characteristic *plateau*. The qualitative dependence of predictions of the two diagrams for the photoelectron energy spectrum has been analysed approximately first by Becker *et al* [21, 22] and Lewenstein *et al* [122]; a typical result of such calculations is displayed in figure 3.

There is no difficulty in principle, but somewhat lengthy calculations are usually needed to evaluate the second-order (rescattering) diagram. The main contribution of the rescattering amplitude arises from the spatial domain in the vicinity of the atomic nucleus. We may point out here parenthetically that often this led one to estimate qualitatively some features

of the rescattering amplitude by an *ad hoc* simplification of the long range (Coulombic) atomic potential by a short-range (or even zero-range) model potential. Because of their simplicity different short-range model potentials have been considered extensively in the past for investigation of electron detachment (or ionization) in intense laser fields. For example, a zero-range delta potential was used by Nikishov and Ritus [153], Manakov and Rapoport [131], Faisal [56–58], Shakeshaft [194], Muller *et al* [148], and more recently by Becker and collaborators [21, 22, 163, 127, 105], and by Starace, Manakov and collaborators [28, 132], or equivalent boundary conditions were used by Faisal and Chen *et al* [54, 34]; short-range separable potentials have been used for intense-field ionization problems by Faisal and collaborators [56, 57, 59, 62], Kamiński [98] and Lewenstein *et al* [123], and screened Coulomb potentials have been used e.g. by Faisal and Becker [66] and by Milosevic and Ehlotzky [136] which avoided the singularity resulting from the long-range Coulomb interaction.

A number of phenomena associated with the 'rescattering' mechanism in above-threshold ionization processes have been analysed by several authors using various approximations to estimate the contributions of the first- and the second-order amplitudes. The investigated themes have been the appearances of anomalous structures (rings) in the angular distributions of above-threshold ionization (e.g. [21, 123, 22, 127]), effects of different forms of the model atomic potentials on the energy plateau (e.g. [136–138, 73]), ATI in bichromatic fields (e.g. [139]), ellipticity effects in high-order ATI (e.g. [106, 164]), role of the so-called 'quantum orbits' (e.g. [106, 107, 189]), interference effects in the photoelectron spectrum, (e.g. [105, 175]), 'enhancements' phenomenon [149] of groups of high-order ATI peaks near channel closings (e.g. [165, 109]) and the effect of rescattering in above-threshold detachment from negative ions [142, 78]. As an example of the numerous works in this context, a comparison between the results of S-matrix calculations by Milošević *et al* [142] and the experimental data obtained by Kiyan and Helm [101] for the energy spectrum of electrons from the detachment of F^-, in the direction of the laser polarization, is shown in figure 4. We point out that a more detailed discussion of the various approximate estimates of the rescattering amplitude, specially by stationary-phase approximation, and for different model potentials, as well as their application to above-threshold ionization, can be found in two recent reviews [24, 142].

4.6. Relativistic S-matrix theory of single ionization

Advent of very intense laser sources at near infrared (Ti-sapphire laser) and shorter than optical wavelengths (free-electron laser, FEL) has stimulated relativistic investigations of laser-atom interaction dynamics in intense fields most significantly within the framework of the Dirac theory. Thus, for example, reinvestigations of spinor-electron wavepacket motion (e.g. [186, 187]), Klein paradox [111], bound-state spin-oscillation [207], Mott scattering (e.g. [31, 200, 158]) and Möller scattering [159] have revealed new features of relativistic dynamics in intense-fields. As noted already, ionization is the most ubiquitous phenomenon that can occur during interaction of atomic systems with 'super-intense' laser fields. For such fields the ponderomotive energy of the electron becomes comparable to or greater than its rest mass energy. Consequently motion of the electron unavoidably becomes relativistic in the field even when the unperturbed motion in the initial state might be non-relativistic. Thus for $U_p \geqslant mc^2$ one ought to use a relativistic formulation of the problem within the Dirac theory. S-matrix formulation of intense-field ionization within the Dirac theory has been discussed in details by Reiss [183]. More recently, the non-relativistic IMST approach (see, section on IMST above) has also been extended to the Dirac relativistic case [70]. We merely note here
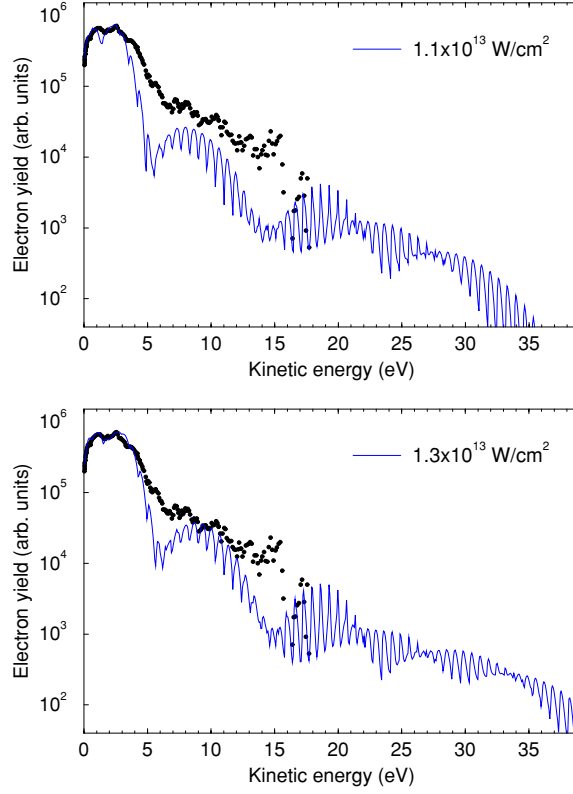
Figure 4. Comparison of *S*-matrix calculations (lines, [143]) for the energy spectrum from electron detachment of F$^-$ at two different peak intensities with the experimental data of Kiyan and Helm [101] at 1.1×10^{13} W cm^{-2} (from [143]. Copyright 2003 by the American Physical Society).

that the method of derivation of the relativistic IM*S*T series is analogous to that discussed in the non-relativistic case, except that the non-relativistic Volkov Green's function has to be replaced by the relativistic Feynman Volkov-propagator that satisfies the Stueckelberg–Feynman boundary condition, which simultaneously accounts for the forward (electron) and backward (positron) propagation in time. Various forms of Feynman Volkov-propagator are available (see, e.g. [26, 89]). We note here another form which is particularly suitable for a diagrammatic treatment of relativistic intense-field problems in direct analogy with the usual (weak-field) Feynman approach. This is provided by the following Floquet representation of the Feynman Volkov-propagator as in [63]:

$$G^0_{n,n'}(p) = \sum_{N=-\infty}^{\infty} \phi_{n-N}(p) \frac{\not{P}_N + m}{P_N^2 - m^2 + \mathrm{i}0} \phi_{n'-N}(p), \qquad (54)$$

where

$$\phi_{n-N}(p) = (1 + B_n(p)) J_{n-N}(a_p, b_p), \qquad (55)$$

$B_n(p) = \mathrm{e} \frac{\not{\kappa}\not{a}}{4\kappa \cdot p} (s_n^+ + s_n^-), a_p = -\frac{ep \cdot a}{2\kappa \cdot p}, b_p = \frac{-e^2 a^2}{8\kappa \cdot p}; s_n^\pm$ merely shifts the index n by ± 1 on functions on which it operates; the shift operators are direct semi-classical analogues of the photon annihilation and creation operators in the quantum number state representation of the field, and $P_N = P - N\kappa$, where κ is the photon momentum. Note that this expression has
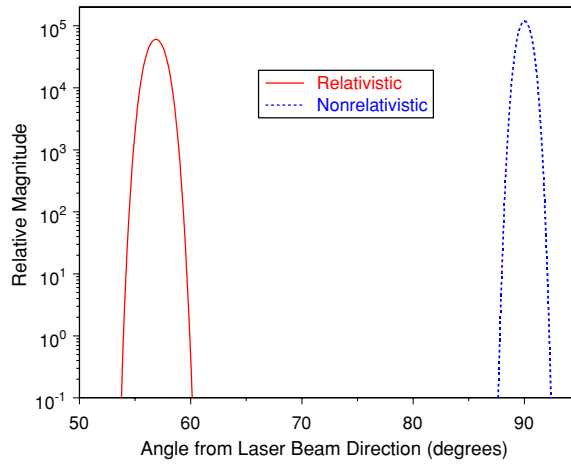
Figure 5. Angular differential rates with emission angles from the direction of the propagation of the beam at a frequency of 0.125 au and an intensity of 5.9 au. A comparison is shown between the results of the relativistic calculation (solid line) and the non-relativistic limit (dashed line), cf [40], reproduced with permission of the authors.

the same form as that of the usual Feynman propagator of a free electron, except that the plane wave Dirac spinor is replaced by the Dirac–Volkov spinor (in momentum space) defined by equation (55).

We point out that the *leading* terms of both the series derived by Reiss's approach or by the relativistic IMST approach are identical, and correspond exactly to the non-relativistic KFR model in the Schrödinger case. But the two series differ term by term from the second term onwards, and a flexibility of the relativistic IMST series analogous to that in the non-relativistic case could be seen to occur.

The relativistic KFR-formula for the transition amplitude for ionization from a bound-state $\psi_{1s}^{(s)}(\mathbf{r}, t)$ of spin s into the Dirac–Volkov continuum states $\psi_{\mathbf{p}}^{(s')}(\mathbf{r}, t)$ of spin s', where $(s, s') = $ u (up) or d (down), is given by

$$S_{s \to s'} = -\mathrm{i} \int_{-\infty}^{\infty} \langle \bar{\psi}_{\mathbf{p}}^{(s')}(t) | \frac{1}{c} \gamma^{\mu} A_{\mu} | \psi_{1s}^{(s)}(t) \rangle \, \mathrm{d}t. \tag{56}$$

Within the above formula, Reiss and collaborators have investigated the differential and the total ionization rates of ground state Dirac H-atom at different laser parameters and polarizations. In figure 5 we show a typical result of their calculations of the angular distribution of the ionized electrons in a circularly polarized field [40]. They are compared with the corresponding result of the non-relativistic case. An interesting difference between the Dirac and the Schrödinger results can be seen to consist of a clear shift of the Dirac angular distribution to the lower angles compared to the Schrödinger case while its shape and size remain virtually unchanged. The shift could be thought of as due to the general relativistic tendency to 'focus' the emitted electrons towards the light propagation direction with increasing velocity. In figure 6 we show the calculated results [40] for the total ionization rates as a function of laser intensity (for circular polarization). It shows a near equality of the relativistic (solid lines) and the non-relativistic (dashed lines) calculations for the total rates. Note the counter intuitive tendency of the rates to *decrease* with increasing intensities.
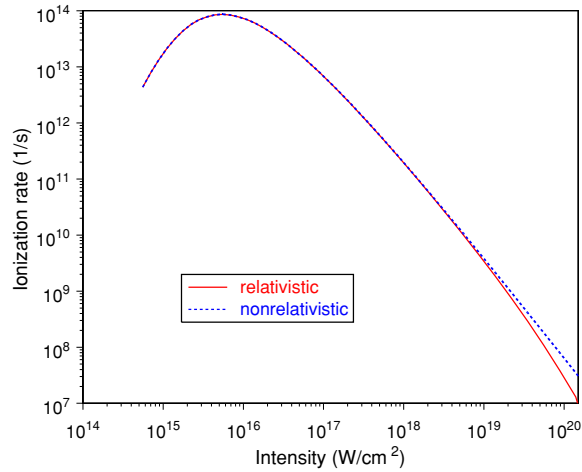
Figure 6. Ionization rates as a function of the laser intensity $\omega = 1/8$ au. A comparison is shown between the results of the relativistic calculation (solid lines) and the non-relativistic limit (dashed lines), cf [40], reproduced with permission of the authors.
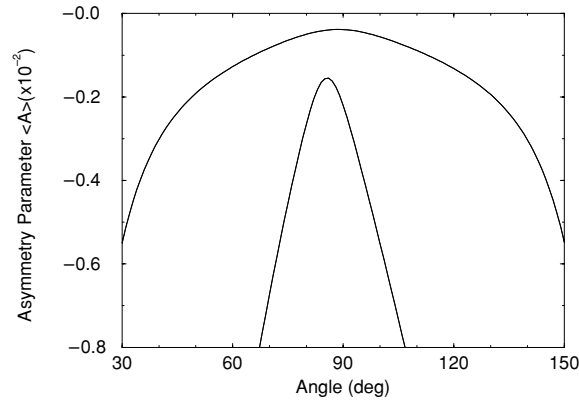
Figure 7. Intensity-dependent ensemble averaged asymmetry parameter $\langle A \rangle$ versus electron emission angle; $\omega = 1.55$ eV, $I = 10^{16}$ W cm^{-2} (outer curve) and $I = 10^{17}$ W cm^{-2} (inner curve), cf [69].

Since spin is essentially relativistic in nature, the relativistic S-matrix theory is expected to provide interesting insights in the spin response of atoms during ionization in an intense field. Recently, spin-resolved electron currents from ionization of Dirac H-atoms have been investigated by Faisal and Bhattacharyya [69] using the relativistic KFR-amplitude, equation (56). It has revealed a remarkable *asymmetry* between the up-spin current and the down-spin current from an ensemble of H atoms subjected to intense circularly polarized laser fields. Figure 7 shows a typical result of the *asymmetry parameter* $\langle A \rangle$, defined as the ensemble averaged difference of the up-spin and down-spin electron currents normalized by their sum, as a function of the angle of emission of the electrons, at two intensities, $I = 10^{16}$ W cm^{-2} (outer curve), and $I = 10^{17}$ W cm^{-2} (inner curve), at a Ti-sapphire laser frequency $\omega = 1.55$ eV. The negative sign of $\langle A \rangle$ shows that the spin-down current is greater

than the spin-up current at all angles. Interestingly, this asymmetry survives the ensemble average of the atoms populated equally in the degenerate up-spin and down-spin sub-states of the ground state. The asymmetry also survives when the photon momentum is negligible (or identically put equal to zero, as in the dipole approximation), which implies that it survives even when the magnetic component of the laser field in the laboratory is negligible. Furthermore the asymmetry remains non-zero when the atomic spin–orbit interaction is absent (as in the bound 1s-state as well as in the Volkov-continuum state). Physically speaking, the spin flip occurs due primarily to (motional) magnetic field generated by the Lorentz transformation of the electric field of the laser in the laboratory, in the moving frame of the emitted electron; the asymmetry arises from the dominance of the spin-flip rates opposite to the photon helicity over that along it [69].

Before concluding this short section on relativistic ionization, we may point out that a tunnel formula for relativistic ionization rate of a bound Dirac electron has recently been proposed by Milosevic *et al* [141].

4.7. High harmonic generation

Besides ionization, an important single-active-electron process is HHG. We note that usually the harmonic generation problem is discussed either in terms of the susceptibility tensors and/or the expectation value of the dipole length or acceleration operators. Nevertheless, as for any other process in quantum world high-harmonic generation in intense fields can be formulated [60] directly in terms of the probability amplitude of the process ([55], p 42). IM$\mathcal{S}$T provides a systematic *ab initio* procedure to generate and investigate these amplitudes. A coherent harmonic of the nth order is associated with the transition amplitude for net absorption of n laser photons by an electron from the ground state of the atom and its return to the ground state again with the emission of a single harmonic photon with an energy $\Omega = n\omega$ into the vacuum mode. The total Hamiltonian of the system can be written conveniently, in which the vacuum field interaction is represented in the intermediate picture ([55], section 6.7), as

$$H = \left(\frac{1}{2} \left(\hat{p} - \frac{A(t)}{c} \right)^2 + V_a(r) \right) + (\hat{V}(t) + h.c.), \tag{57}$$

where

$$\hat{V}(t) = -\frac{\hat{p} \cdot A^+(t)}{c} |1_\Omega\rangle \langle 0_\Omega|. \tag{58}$$

The vector potential of the emitted photon

$$A^+(t) = \epsilon_\Omega \sqrt{\frac{2\pi c^2}{\Omega}} \exp(-i\Omega t) \tag{59}$$

is directed along the unit polarization vector of the emitted radiation ϵ_Ω. Clearly for this process the initial and the final atomic reference Hamiltonians are the same:

$$H_i^0 = H_f^0 = \frac{\hat{p}^2}{2} + V_a(r), \qquad V_i(t) = V_f(t) = V_L(t) + (\hat{V}(t) + h.c.). \tag{60}$$

The intermediate partition in a strong field is

$$H_0(t) = \frac{1}{2} \left(\frac{\hat{p} - A(t)}{c} \right)^2 \qquad \text{and} \qquad V_0(t) = V_a(r). \tag{61}$$

The lowest non-zero contributions in the S-matrix expansion for the high harmonic generation (using the above partitions) appear in the second order. The resulting two lowest
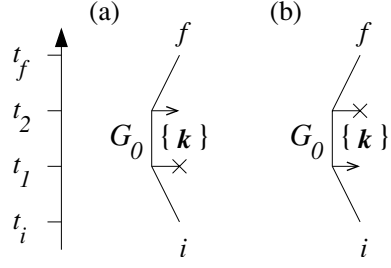
Figure 8. Diagrams generated by the IMST for high-harmonic generation.

order HHG diagrams are shown in figures 8(a) and (b). In this representation the initial state of the system is given by $|\phi_i(t)\rangle|0_\Omega\rangle$, where the atom is in the ground state $|\phi_i(t)\rangle$ and no harmonic photon is present in the vacuum mode, $|0_\Omega\rangle$. According to the diagram in panel (a) (reading from bottom to top) the electron propagates from the initial state, interacts with the laser field at $t = t_1$ and goes into the intermediate Volkov states, and then at a later time $t = t_2$ the Volkov electron recombines with the parent ion (in the same atomic state as initially) and a harmonic photon of energy $\hbar\Omega$ is created in the state $|1_\Omega\rangle$. Thus the final state of the system is $|\phi_f(t)\rangle|1_\Omega\rangle$. The diagram in panel (b) describes the same process but in the reversed order: the atom emits the harmonic photon first, goes into the Volkov states and returns to the ground state by interaction with the laser field. The associated analytical expression generated by IMST is easily written by reading the diagrams from bottom to top. Thus the diagrams 3(a) and (b) generate the following sum of the two amplitudes:

$$
\begin{aligned}
(S-1)_{fi}(t_f, t_i) = -\mathrm{i} \int \mathrm{d}\boldsymbol{k} \int_{t_i}^{t_f} \mathrm{d}t \int_{t_i}^{t_f} \mathrm{d}t' &\left[\langle \phi_i(\boldsymbol{r};t)| \langle 1_\Omega| \hat{V}(t)|0_\Omega\rangle |\phi_{\boldsymbol{k}}(\boldsymbol{r})\rangle \right. \\
&\times \exp\left(\mathrm{i}\int_{t'}^{t} \mathrm{d}\tau E_k(\tau)\right) \langle \phi_{\boldsymbol{k}}(\boldsymbol{r})|V_L(t')|\phi_i(\boldsymbol{r};t')\rangle \Big]_a \\
&+ \left[\langle \phi_i(\boldsymbol{r};t)|V_L(t)|\phi_{\boldsymbol{k}}(\boldsymbol{r})\rangle \exp\left(\mathrm{i}\int_{t'}^{t}\mathrm{d}\tau E_k(\tau)\right) \right. \\
&\times \langle \phi_{\boldsymbol{k}}(\boldsymbol{r})| \langle 1_\Omega|\hat{V}(t')|0_\Omega\rangle|\phi_i(\boldsymbol{r};t')\rangle \Big]_b,
\end{aligned}
\tag{62}
$$

where the Volkov Green's function is given by equation (32). We expand the exponents using the Jacobi–Anger relation, perform the integrations over the coordinates, and the two integrations over the time variables analytically and get

$$
(S-1)_{fi}(\infty, -\infty) = -2\pi\mathrm{i} \sum_{n=-\infty}^{\infty} \delta(n\omega - \Omega) \int \mathrm{d}\boldsymbol{k}\big(T_a^{(n)}(\boldsymbol{k}) + T_b^{(n)}(\boldsymbol{k})\big),
\tag{63}
$$

where

$$
T_a^{(n)}(\boldsymbol{k}) = \sqrt{\frac{2\pi c^2}{\Omega}}(\boldsymbol{\epsilon}_\Omega \cdot \boldsymbol{k}) \sum_{s=-\infty}^{\infty} (s\omega - U_p)\frac{J_{n+s}(a_k, b)J_s(a_k, b)}{\frac{k^2}{2} + E_B + U_p - s\omega + \mathrm{i}0}|\tilde{\phi}_i(\boldsymbol{k})|^2
\tag{64}
$$

and,

$$T_b^{(n)}(\boldsymbol{k}) = \sqrt{\frac{2\pi c^2}{\Omega}} (\boldsymbol{\epsilon}_\Omega \cdot \boldsymbol{k}) \sum_{s=-\infty}^{\infty} \left((n+s)\omega - U_p\right) \frac{J_{n+s}(a_k, b) J_s(a_k, b)}{\frac{k^2}{2} + E_B + U_p - \Omega - s\omega + \mathrm{i}0} |\tilde{\phi}_i(\boldsymbol{k})|^2.$$
(65)

It is useful to note that $T_b^{(n)}$, in the presence of the delta function in equation (63), can be rewritten by shifting the summation index $s \to (s - n)$. We note here parenthetically that in some S-matrix type formulations of the HHG amplitude, to be found in the literature, the amplitude $T_b^{(n)}$ associated with the second diagram, figure 8(b), is absent and hence incomplete within the same order.

The present IMST formulation of the HHG amplitude, equation (62), is in fact a velocity gauge equivalent of the well-known Lewenstein model of HHG in the length gauge [122]. The latter uses the *classical* Larmour formula for the emission of the spontaneous radiation and the quantum *expectation* value of the dipole operator in the laser field. In fact the present procedure when carried out in the length gauge reproduces the same result of the dipole expectation value as well. Clearly, therefore, the expectation value procedure and the transition amplitude procedure within IMST are consistent with each other (as they should be), provided *both* the amplitudes associated with the diagrams 3(a) and (b) are taken into account. The absolute rate of emission of the nth harmonic is now easily written in terms of the sum of the two T-matrices above,

$$\frac{\mathrm{d}\Gamma_{\mathrm{HHG}}^{(n)}}{\mathrm{d}\hat{\boldsymbol{K}}_\Omega} = \frac{(2\pi)^2 \alpha \Omega_n}{c^2} \left| \int \mathrm{d}\boldsymbol{k} (\boldsymbol{\epsilon}_\Omega \cdot \boldsymbol{k}) |\tilde{\phi}_i(\boldsymbol{k})|^2 \right.$$

$$\left. \times \sum_{s=-\infty}^{\infty} (s\omega - U_p) J_s(a_k, b) \frac{J_{s+n}(a_k, b) + J_{s-n}(a_k, b)}{\frac{k^2}{2} + E_B + U_p - s\omega + \mathrm{i}0} \right|^2,$$
(66)

where the HHG wave number $K_\Omega = \Omega/c$, and $\mathrm{d}\hat{\boldsymbol{K}}_\Omega$ is the element of solid angle in the direction of the propagation vector of the harmonic radiation, $\Omega_n = n\omega$ and $\alpha \approx 1/137.036$ is the fine structure constant.

Numerical calculations of the single atom HHG spectra using various atomic models and approximations have been made extensively in the past (e.g. [122, 24, 142, 116]). In figure 9 typical results of calculations within the Lewenstein model [122] are presented for a model atomic system with $I_p = 20$ au and $U_p = 10$ au (open squares) and $U_p = 20$ au (filled squares). Large values of I_p and U_p have been chosen in order to demonstrate that the exact quantum mechanical value for the cut-off of the spectrum slightly differs from the phenomenological value $3.17U_p + I_p$. Recent detailed reviews of various approximations and computations can be found in [47, 48, 24, 142].

4.8. General properties of high harmonic radiation

In this subsection, we discuss a number of characteristics of HHG radiation which should hold generally for any atom when interacting with an intense linearly polarized laser field. First we draw two general conclusions [60, 61] about the nature of the basic single-atom HHG radiation, namely (I) only odd harmonics contribute to HHG from atoms prepared in a state with a *definite* parity, and (II) the HHG and ATI probabilities are *correlated* to each other essentially in the following way: the higher order HHG are related to the *on-shell* ATI amplitudes and the lower order HHG to the *off-shell* ATI-amplitudes. These can be illustrated explicitly from equation (66), as follows.
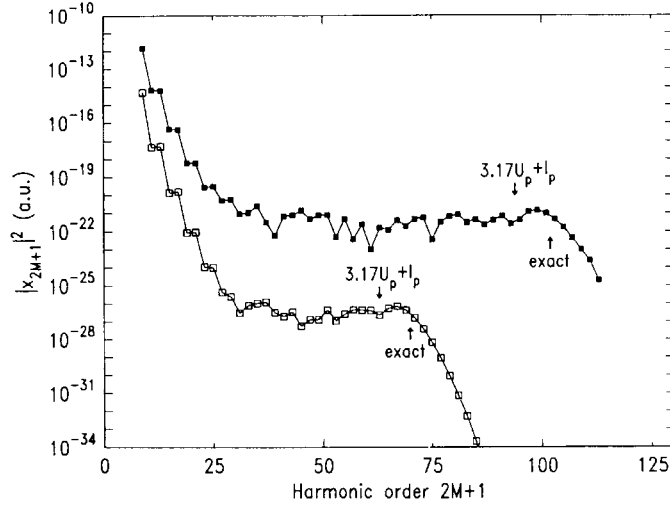
Figure 9. Typical spectra of high-harmonic generation calculated using the dipole expectation value given by the Lewenstein model (from [122]. Copyright 1994 by the American Physical Society).

I. We may change the integration vector k in equation (66) to $-k$ and use the parity property of the generalized Bessel function, namely $J_n(-a_k, b) = (-1)^n J_n(a_k, b)$, to get

$$\frac{d\Gamma_{HHG}^{(n)}}{d\hat{K}_\Omega} = \left| \frac{1 + (-1)^{n+1}}{2} \right|^2 \frac{d\Gamma_{HHG}^{(n)}}{d\hat{K}_\Omega}. \tag{67}$$

Thus, it survives only for n odd; clearly $(1 + (-1)^{n+1})/2 = 0$ for n even, and 1 for n odd.

II. We note that the denominators in the two terms in equation (66) can be written, using the Plemlej resolution as

$$\frac{1}{\epsilon_k - s\omega \pm i0} = \text{P.V.} \left(\frac{1}{\epsilon_k - s\omega} \right) \mp i\pi\delta(E_k - s\omega), \tag{68}$$

where $\epsilon_k = k^2/2 + I_p + U_p$ and P.V. stands for the principal value. The delta part is non-vanishing only for the on-shell transitions in the ATI continuum of the electron, corresponding to the ATI amplitudes of sth orders but weighted quadratically by the momentum distribution in the initial state. Note that each high harmonic of a given order n arises from the sum of such weighted ATI contributions from *all* allowed ATI thresholds. The off-shell P.V. part is specially responsible for the lower order harmonics with HHG-photon energy *less* than the ionization threshold energy, where the on-shell ATI-amplitudes do not contribute. We point out that the question of the relation between the above-threshold ionization and HHG has been a subject of much interest from the very beginning of the theoretical considerations about the process, and as such has been considered from the earliest time on by Shore and Knight [196], Eberly and collaborators [46], Faisal [60, 61], Becker and collaborators [20, 23], Schafer and collaborators [190], as well as more recently, by Kuchiev and Ostrovsky [115–118] among others.

III. Another question of much interest is the relation between the single-atom HHG emission spectrum and the *many-atom* emission spectrum, where only the latter is commonly measured in a gas medium. In fact, it is the *many-atom* contribution that leads to a coherent enhancement of the single-atom HHG emissions. This makes it both readily observable and useful for

applications. Thus the problem of *phase-matching* of the HHG radiation from different atoms is of considerable significance. The basic physics of the phase matching of the emitted harmonics from an ensemble of randomly distributed atoms situated at the positions $R_j (j = 1, 2, 3 \ldots N_a)$, and the associated coherent enhancement of the HHG radiation can be understood quite simply as shown some time ago by Faisal [60, 61]. Thus, assuming that the individual atomic centres are located at R_j, the phase of the transition amplitude with respect to the atomic centre at R_j can be obtained by simply shifting the initial phase of the vector potential of the laser such that $\exp(-i\omega t) \rightarrow \exp(-i(\omega t - k_\omega \cdot R_j))$ (and the same for its complex conjugate). Note that we are still using dipole approximation with respect to the position, r_j, of the electron measured from its atomic centre, or $|(r_j - R_j) \cdot k_\omega| \ll 1$. The same transformation holds for the vector potential of the harmonic radiation, $\exp(-i\Omega t) \rightarrow \exp(-i(\Omega t - K_\Omega \cdot R_j))$. Then proceeding exactly as before and adding the single-atom HHG amplitudes emitted by the individual atoms we get the many-atom *amplitude* which differs from the single-atom amplitude, equation (62), by the simple *factor* [60]:

$$\sum_{j=1}^{N_a} \exp(i(nk_\omega - K_\Omega) \cdot R_j). \tag{69}$$

For a random distribution of a large number, N_a, of gas atoms, this sum becomes negligible by destructive interference if $nk_\omega \neq K_\Omega$, and equals N_a, for $nk_\omega = K_\Omega$. Hence the emission *probability* increases coherently as N_a^2 (over the single-atom case) when the phase is matched exactly, $\Delta K = nk_\omega - K_\Omega = 0$. This is nothing but the requirement of momentum conservation between the n absorbed laser photons and the emitted HHG photon.

For a non-uniformly distributed medium this expression takes the form [61]

$$\left| \int dR N_a n(R) \exp(i(nk_\omega - K_\Omega) \cdot R) \right|^2 = N_a^2 \mathcal{F}(nk_\omega - K_\Omega), \tag{70}$$

where $n(R)$ is the 'density function per atom', and $\mathcal{F}(nk_\omega - K_\Omega)$, which is given by the square of the Fourier transform of $n(R)$, is the phase-matching function. The latter peaks when $nk_\omega \approx K_\Omega$. Therefore for a non-uniform medium, $n(R)$, certain tolerance range around $nk_\omega \approx K_\Omega$ is permitted that allows an equivalent tolerance in the refractive index variation in the medium. Thus, in general the many-atom signal is enhanced coherently as the *square* of the number of atoms (or pressure), under the condition of near momentum conservation between the n laser photons and the emitted harmonic photon. This also shows that the HHG radiation propagates preferentially along the same direction as the incident laser beam. Furthermore, as can be expected from equation (66), the main contribution of the harmonic intensity is expected to come (assuming a linearly polarized laser field) from those electrons whose *intermediate* momenta are parallel to the laser polarization axis. Hence the strongest emission of the harmonic radiation, according to formula (66), is expected to have its polarization ϵ_Ω parallel to the laser polarization direction ϵ_ω. These general characteristics speak for the highly coherent nature of the HHG radiation.

IV. We note further that in the presence of intense fields there is nothing that can prevent the emission of discrete spontaneous radiation lines at frequencies $\Omega = (E_i + n\omega - E_f)$, where E_i and E_f are the eigenenergies of the ground (initial) state and any other excited (final) state of the atom, respectively. In general, however, these frequencies are *not* commensurate with any harmonic multiple of the fundamental laser frequency. Therefore, they are not enhanced by stimulated emission by the (high density) laser photons, at the single-atom level. They are also not enhanced by coherent phase matching in the medium, at the many-atom

level, since the non-vanishing frequency mismatch in the time domain, $\exp(i\Delta t)$, where $\Delta = (E_i - E_f)/\hbar \neq 0$, tends to wash out the coherence by destructive interference, during the usual observation time. Thus, the emission at such 'hyper-Raman' frequencies is expected to be much weaker (if observed) compared to the intensities of comparable HHG frequencies.

Before concluding this section we may add that most of the characteristic general properties of the HHG radiation discussed above have been found to be generally consistent with the experimental observations of the phenomenon [135, 71, 125]. For a detailed quantitative understanding of the specific experimental signals as well as for possible technological applications of HHG in a given dielectric and/or ionizing medium, one often needs to consider the propagation of the full field amplitude and the full phase through the medium. They can be obtained from solutions of the *coupled* Maxwell–Schrödinger equations of the combined system of the atom and the field. Considerable progress has been made recently both experimentally and computationally in this regard; they are discussed in a recent review of the subject [188].

5. Two-active-electron processes in atoms: double ionization

Intense-field physics has revealed new aspects of many-body electron–electron correlation in atomic systems that are neither observed in ground state atoms nor in the usual photo-excitation or photo-ionization processes. As discussed above, single ionization and high-harmonic generation in atoms can be satisfactorily explained within the single-active-electron (SAE) approximation, where only the outermost electron is assumed to be affected by the laser field. Note that this picture neglects the inter-electron correlation between the electrons of the atom. In the absence of correlation, the double ionization process would imply a *sequential* mechanism in which the neutral atom is first ionized and then the cation would be further ionized independently. This hypothesis has been disproven by the observation of enormously excessive double and multiple ionization yields in intense fields when they were compared with the prediction of the sequential mechanism. We show a typical example of intense-field double ionization of He in figure 10(a) in intense near-infrared wavelength laser fields. Here both the single ionization and the double ionization yields versus the laser intensity are shown as observed in an experiment with a Ti:sapphire laser ($\lambda = 780$ nm) by Walker *et al* [208]. For intensities below 10^{15} W cm^{-2} a strong enhancement of the He^{2+}-yield by many orders of magnitude can be seen to occur over the prediction of the sequential mechanism (dashed line, Coulomb-corrected KFR calculation, or nearly equal SAE simulation). There is also a characteristic 'knee' structure to be seen on the double ionization curve below the saturation intensity for the single ionization process[7].

As it will be seen below, an inelastic scattering by the Volkov electron in the intermediate (virtual) state can cause a second electron from the parent atom to be ejected. This is the counterpart of the elastic 'rescattering' in the single ionization case and the 'recombination' phase (into the parent atomic state) of high-harmonic emission process discussed above. The *inelastic* rescattering process has turned out to be the dominant process for double ionization of atoms in intense infrared (or near-infrared) laser frequencies [9, 10]. In fact analyses of the IMST diagrams generated by the leading terms of the many-body S-matrix theory for all the three processes (high-energy part of the ATI, HHG and *non-sequential* double ionization (NSDI)) have provided the first quantitative quantum mechanical justification in favour of the 'rescattering' hypothesis, originally advanced by Corkum and others in the present context

[7] The saturation intensity is defined as the intensity at which the effective ionization probability is unity. From the double logarithmic yield versus intensity curve it may be crudely estimated to be the intensity at which the slope of the yield from the lower intensity domain intersects with the slope from the upper intensity domain.
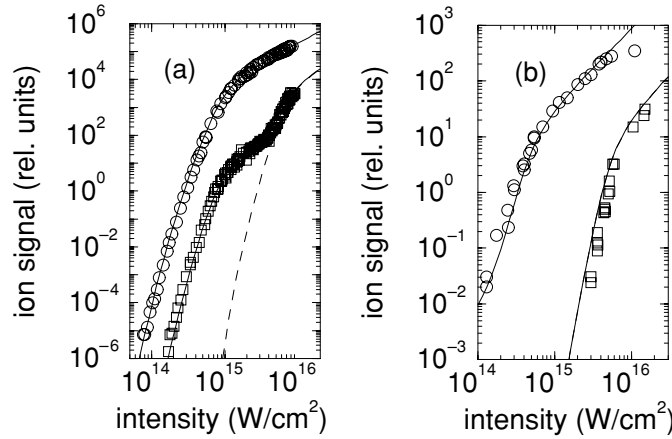
Figure 10. Measured He ion yields for linear polarized (a) 780 nm [208] and (b) 248 nm [33] laser light. Results of S-matrix calculations (cf [10]) are shown as solid lines; contribution from the sequential channel is shown by dashed lines. Note the strong enhancement of the double ionization yield, over the sequential prediction at 780 nm and its absence at 248 nm. Note that at 248 nm for the He^{2+} yield, the dashed and solid lines cannot be distinguished in the figure.

(e.g. [38, 190]). More generally, the IMST analyses have also revealed that in intense fields the mechanism of double ionization process *depends* qualitatively on the wavelength domain of the laser field [10]. Thus while at the near infrared wavelengths the mechanism of non-sequential ejection (NSDI) of the two electrons dominates, at the UV wavelength (e.g. $\lambda = 248$ nm) there is no sign of the presence of the non-sequential process. As can be seen from the data presented in figure 10(b), the experimental results at 248 nm obtained by Charalambidis *et al* [33] in fact have been shown by Becker and Faisal [10] to agree with the prediction of the sequential mechanism of double ionization, which were calculated using the direct ionization amplitude from the first-order IMST.

In this section, we shall discuss the application of IMST to the double ionization process with terms up to the second order and analyse the process diagrammatically and quantitatively. In fact diagrams will be identified that correspond to different mechanisms proposed in the literature. We shall consider results of ionization yields as well as that of recent coincidence experiments. The dominant diagram for the NSDI is identified as the inelastic rescattering (or correlated energy-sharing, CES) diagram. Finally, we shall briefly consider extensions of the CES diagrams to higher orders and discuss a model formula for obtaining the yields of double *and* multiple ionization.

5.1. Diagrams and mechanisms

We discuss the problem of double ionization of a He atom in an intense laser field. He atom being the simplest atom that permits double ionization, is a good system in which to study both experimentally and theoretically the role of correlation in intense fields. The Schrödinger equation of the system is given by

$$i\frac{\partial}{\partial t}\Psi(\boldsymbol{r};t) = \left(\frac{\hat{\boldsymbol{p}}_1^2 + \hat{\boldsymbol{p}}_2^2}{2} - \frac{(\hat{\boldsymbol{p}}_1 + \hat{\boldsymbol{p}}_2)\cdot \boldsymbol{A}(t)}{c} + \frac{A^2(t)}{c^2} - \frac{Z}{r_1} - \frac{Z}{r_2} + \frac{1}{r_{12}}\right)\Psi(\boldsymbol{r};t), \qquad (71)$$

where $r_{12} = |\boldsymbol{r}_1 - \boldsymbol{r}_2|$. In the application of IMST to the double ionization process the initial-state and final-state Hamiltonians, $H_i^0(t)$ and $H_f^0(t)$, are chosen as to correspond to the choice of the initial unperturbed two-electron bound state (at the beginning of the process)
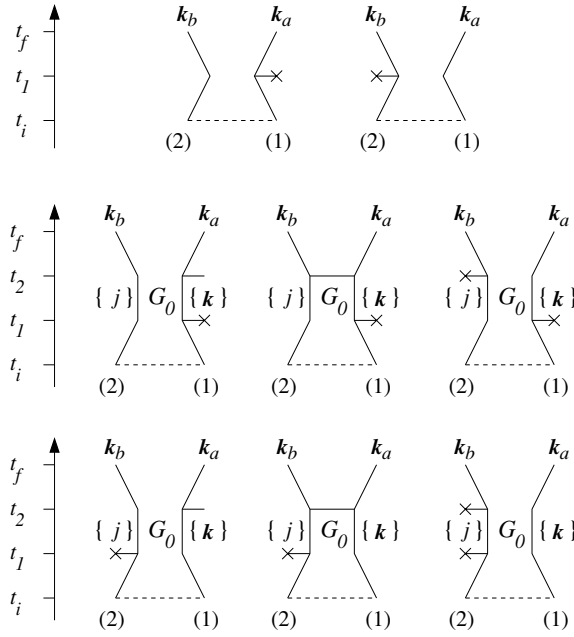
Figure 11. Two diagrams in first order (upper row) and six diagrams in the second order (middle and lower rows) that are generated by the first two leading terms of IMST for the double ionization process.

and the state of the two ejected electrons in the field (at the end of the process), respectively [13, 18]:

$$H_i^0 = \frac{\hat{p}_1^2 + \hat{p}_2^2}{2} - \frac{Z}{r_1} - \frac{Z}{r_2} + \frac{1}{r_{12}}, \qquad V_i(t) = -\frac{(\hat{p}_1 + \hat{p}_2) \cdot \mathbf{A}(t)}{c} + \frac{A^2(t)}{c^2} \tag{72}$$

and

$$H_f^0 = \frac{\hat{p}_1^2 + \hat{p}_2^2}{2} - \frac{(\hat{p}_1 + \hat{p}_2) \cdot \mathbf{A}(t)}{c} + \frac{A^2(t)}{c^2}, \qquad V_f(t) = -\frac{Z}{r_1} - \frac{Z}{r_2} + \frac{1}{r_{12}}. \tag{73}$$

The intermediate state propagator, $G^0(t, t')$, is chosen to represent the propagation of one electron in the virtual Volkov states and the other electron in the complete set of states of the residual ion:

$$\left[\mathrm{i}\frac{\partial}{\partial t} - H^0(t) \right] G^0(t, t') = \delta(t - t') \tag{74}$$

with

$$H^0 = \frac{\hat{p}_1^2 + \hat{p}_2^2}{2} - \frac{\hat{p}_1 \cdot \mathbf{A}(t)}{c} + \frac{A^2(t)}{2c^2} - \frac{Z}{r_2} \tag{75}$$

and the associated interaction

$$V_0(t) = -\frac{\hat{p}_2 \cdot \mathbf{A}(t)}{c} + \frac{A^2(t)}{2c^2} - \frac{Z}{r_1} + \frac{1}{r_{12}}. \tag{76}$$

Introduction of these partitions in the intense-field many-body S-matrix theory generates eight Feynman-like diagrams: two from the first order and six from the second term of the IMST series, which are shown in figure 11. The first term provides two symmetric diagrams

shown in the upper row, where the solid lines stand for the evolution of the states of the two active electrons, (1) and (2). According to the first diagram, at the initial time t_i, the two electrons are in the ground state of the He atom; electron correlation is included in the initial atomic state as indicated by the dotted line between the electrons. At a time t_1 one of the two equivalent electrons may interact with the field, absorb a large amount of field energy and leave the atom so quickly that the second electron is 'shaken-off' from the atom. Then the two ejected electrons would propagate in the final state with momenta k_a and k_b in the presence of the field and arrive at the detector(s) at a final time $t_f \to \infty$ where the field is switched off. These two diagrams correspond to the strong-field analogues of the two-electron *shake-off* (SO) process which also occur in double ionization by high frequency photons from much weaker synchrotron radiation sources (e.g. [134]). The SO mechanism has been originally proposed by Fittinghoff *et al* [76] as a possible mechanism for the unusually large NSDI yields observed in a strong laser field.

The second term of the IMST provides a set of six diagrams (the middle and the lowest row of figure 11), of which *only* one dominates, as was shown by Becker and Faisal [9], for the class of experiments performed in the infrared to near-optical wavelengths, and $I > 10^{13}$ W cm^{-2}. Note that there are four diagrams in this set which are 'disjoint' (or show no connection between the electron lines) and therefore they do not contain the effect of electron–electron correlation *during* the double ionization process. We may point out here that the connection at the initial time (dotted line), which stands for the static or ground state correlation, has been found to contribute quantitatively negligibly [9] to the total rate. We also note that one of these four diagrams, namely the one on the right-hand side in the middle row, resembles a sequential double ionization (SDI) mechanism (for a long intermediate time, $t_2 - t_1 > \pi/\omega$) or a 'collective double ionization' (CDI) mechanism (for a short intermediate time, $t_2 - t_1 \to 0$). The latter corresponds to a limiting case associated with the so-called 'collective tunneling' (CT) picture proposed by Eichmann *et al* [49]. Quantitative estimates of these four diagrams have shown that they too do not contribute significantly to the double ionization process in the laser parameter domain of the above experiments. Clearly therefore the SDI, CDI or CT mechanisms of double ionization, associated with the diagrams discussed so far, can be assumed to be unimportant for the process, in the above domain of laser parameters.

The two remaining diagrams (shown in the centre of the middle and the lowest rows) are *conjoint* or have a direct connection line between the two electrons in the intermediate states. They indicate the presence of a *dynamic* electron–electron correlation i.e. which connects the states of the system that are virtually excited by the laser field. The conjoint diagram in the middle row is the CES diagram [65, 9, 10, 13]. According to this diagram, one of the two electrons becomes active first and absorbs a large amount of field energy at a time t_1. At a subsequent time t_2 it interacts with the atomic core and shares its energy with the other electron via the electron–electron correlation operator $1/r_{12}$. Then, both the electrons may emerge together with momenta k_a and k_b in the final state in which they are Volkov-dressed by the field. During the time interval $t_2 - t_1$ the electrons are in the virtual (intermediate set of) states: one electron is in the Volkov state of all virtual intermediate momenta, $\{k\}$, and the other is in the intermediate states of the ion, with all virtual energies $\{E_j\}$. This 'propagator stage' includes an integration over all intermediate time intervals $t_2 - t_1$ which involve *both* short-time ($t_2 - t_1 < \pi/2\omega$) correlation ('on the way out' e–e scattering) as well as 'long-time' ($t_2 - t_1 > \pi/2\omega$) correlation (e–e rescattering). Note, that the physics of the 'correlated energy sharing' or CES diagram, derived from the S-matrix theory, includes the rather analogous concepts of the 'antenna' picture advanced by Kuchiev [112–114] and the classical or semi-classical rescattering picture proposed by Corkum and others [38, 190] as mentioned above. The last diagram of the set is in the middle of the lowest row; it corresponds

to the unlikely event in which the second electron interacts with the laser field while the first electron goes into the intermediate Volkov states. And its contribution is likewise small.

5.2. Analytic rate formulae and coincidence distributions

Recent data of coincidence measurements of the momenta of the two electrons permit one to compare them, at a deeper level than that of the total ion yields, with the prediction of the IMST diagrams for the SO mechanism and the CES (or rescattering) mechanism. And thereby one could clearly determine the importance (or otherwise) of the two competitive mechanisms for the NSDI. It is not difficult to derive, from the respective diagrams, the differential rates of double escape due to the absorption of N photons in a linearly polarized laser field. One gets [18],

$$\frac{\mathrm{d}W_N(\mathbf{k}_a, \mathbf{k}_b)}{\mathrm{d}\mathbf{k}_a \, \mathrm{d}\mathbf{k}_b} = 2\pi\delta\left(\frac{k_a^2}{2} + \frac{k_b^2}{2} + E_{1S} + 2U_p - N\omega\right) |T_N(\mathbf{k}_a, \mathbf{k}_b)|^2, \qquad (77)$$

where T_N stands for the shake-off T-matrix element,

$$T_N^{(SO)}(\mathbf{k}_a, \mathbf{k}_b) = \sqrt{2} \sum_n J_{N-n}\left(\boldsymbol{\alpha}_0 \cdot \mathbf{k}_a; \frac{U_p}{2\omega}\right) J_n\left(\boldsymbol{\alpha}_0 \cdot \mathbf{k}_b; \frac{U_p}{2\omega}\right)$$

$$\times (U_p - (N-n)\omega)\langle \phi_{\mathbf{k}_a}(\mathbf{r}_1)\phi_{\mathbf{k}_b}(\mathbf{r}_2) + \mathbf{k}_a \leftrightarrow \mathbf{k}_b | \phi_{1S}(\mathbf{r}_1, \mathbf{r}_2)\rangle, \qquad (78)$$

or the correlated energy-sharing T-matrix element,

$$T_N^{(CES)}(\mathbf{k}_a, \mathbf{k}_b) = \sum_j \int \mathrm{d}\mathbf{k}\, \frac{1}{\sqrt{2}} \langle \phi_{\mathbf{k}_a}(\mathbf{r}_1)\phi_{\mathbf{k}_b}(\mathbf{r}_2) + \mathbf{k}_a \leftrightarrow \mathbf{k}_b | V_C | \phi_j^+(\mathbf{r}_2)\phi_{\mathbf{k}}(\mathbf{r}_1)\rangle$$

$$\times \sum_n (U_p - N\omega) \frac{J_{N-n}\left(\boldsymbol{\alpha}_0 \cdot (\mathbf{k}_a + \mathbf{k}_b - \mathbf{k}); \frac{U_p}{2\omega}\right) J_n\left(\boldsymbol{\alpha}_0 \cdot \mathbf{k}; \frac{U_p}{2\omega}\right)}{\frac{k^2}{2} - E_j + E_B + U_p - n\omega + i0}$$

$$\times \langle \phi_j^+(\mathbf{r}_2)\phi_{\mathbf{k}}(\mathbf{r}_1) | \phi_{1S}(\mathbf{r}_1, \mathbf{r}_2)\rangle. \qquad (79)$$

Here $\phi_j(\mathbf{r})$ are the intermediate states of the He$^+$ ion, and $\phi_{1S}(\mathbf{r}_1, \mathbf{r}_2)$ is the initial ground-state wavefunction of the He atom. $E_{1S} = 79.02$ eV and E_j are the binding energy of the He ground state and the binding energy of the He$^+$ intermediate state, respectively.

For the actual computations of the full amplitudes, equations (78) and (79), Becker and Faisal [18] performed the six-dimensional integrations over the coordinates analytically, the radial integration in k in $T_N^{(CES)}$ using the pole approximation and the remaining integrations over the angles of $\mathbf{k}$, as well as the sum over n, numerically. It was also found that the sum over the intermediate ionic states, j, in $T_N^{(CES)}$ could be essentially restricted to the ionic ground state only, since this contribution dominated by orders of magnitude over that from an intermediate excited state [9].

We note that the double ionization amplitude, equation (79), is sometimes estimated by introducing additional mathematical and/or physical approximations. For example, a stationary-phase approximation has been used for the integrations over the time variables and the electron momentum in the intermediate states by Goreslavskii and Popruzhenko [174] and by Kopold *et al* [108]. This approximation can reduce the computation time of the rates considerably compared to the full calculation mentioned above as long as only a few stationary points contribute significantly to the rates. We may note, however, that in these calculations their use of a zero-range contact potential (in place of the physical Coulomb interaction) produces, rather inexplicably, a better agreement with the experimental data than the stationary-phase calculation using the actual Coulomb interaction [81].
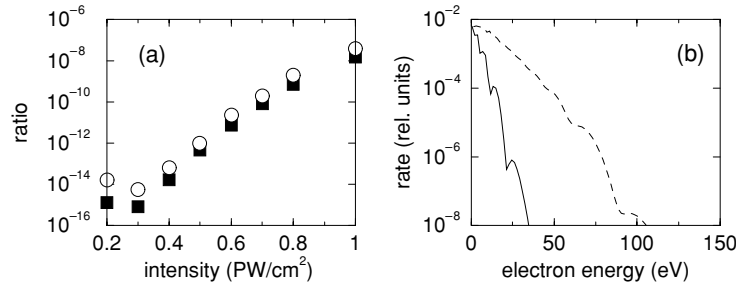
Figure 12. Double ionization of He as a function of the intensity at 780 nm. (a) Ratio of the calculated SO to CES (or rescattering) contributions (filled squares, cf [18]); also shown is the ratio of shake-up (SU or the first excitation) to CES (or rescattering) contributions (open circles). (b) Electron energy spectrum from ionization of He at 780 nm and 4×10^{14} W cm^{-2} (solid line) and 8×10^{14} W cm^{-2} (dashed line). The spectra are rescaled to match near the energy threshold.

In figure 12(a), the ratios of the total ionization rates from the two mechanisms SO and CES (filled squares) are shown as a function of the laser intensity at $\lambda = 780$ nm [18]. Calculations have been performed using the T-matrix elements, equations (78) and (79). The contribution from the CES (rescattering) mechanism clearly dominates by *many orders* of magnitude over that from the SO mechanism at all intensities. The result could be understood qualitatively as follows: the efficiency of the shake-off mechanism depends on the number of initially emitted *fast* electrons that can cause the 'shaking'. But, for low-frequency strong-field ionization, in general, most of the initially emitted electrons are slow. This can be seen from figure 12(b), in which the results of the Coulomb corrected KFR calculations for the ATI spectrum of He at 780 nm and two intensities are shown. Such slow electrons can hardly 'shake' the atom significantly. In contrast, in the correlated energy-sharing (rescattering) mechanism, electrons of any intermediate energy can participate and, hence, the presence of the much larger low-energy fraction that are accelerated by the field before the collision can greatly contribute to the double ionization rate. Also shown in figure 12(a) is the ratio of the rates of the shake-up process to those of CES rescattering mechanism. In the shake-up process the second electron is assumed to be 'shaken-up' to the first excited state in He$^+$ in the final state. The rates for this process too are many orders of magnitude smaller compared to those of the CES rescattering process.

5.3. Analysis of coincidence measurements

Recently, development of multi-electron-ion imaging techniques and their successful combination with femtosecond laser systems with kilohertz pulse-repetition rates have enabled differential measurements on strong-field double ionization of noble gas atoms (He, Ne, Ar and Xe) to be carried out. Coincident measurements of the momentum distributions [211, 144, 212–214, 72, 145, 216] as well as of energy distributions [218, 120, 170, 32] of the ejected electrons produced by double (and triple) ionization provide significant complementary information to the earlier data of the total ionization yields. A detailed discussion of the experimental techniques and results of some of these measurements can be found in the recent review by Dörner *et al* in [45].

In figure 13 the experimental data (circles) for the momentum distributions of He^{2+} obtained by Weber *et al* [211] are compared with the results of S-matrix calculations at $\lambda = 780$ nm and 6.6×10^{14} W cm^{-2}: (a) parallel momentum distribution, and (b) perpendicular momentum distribution. Note that under the condition of the experiment
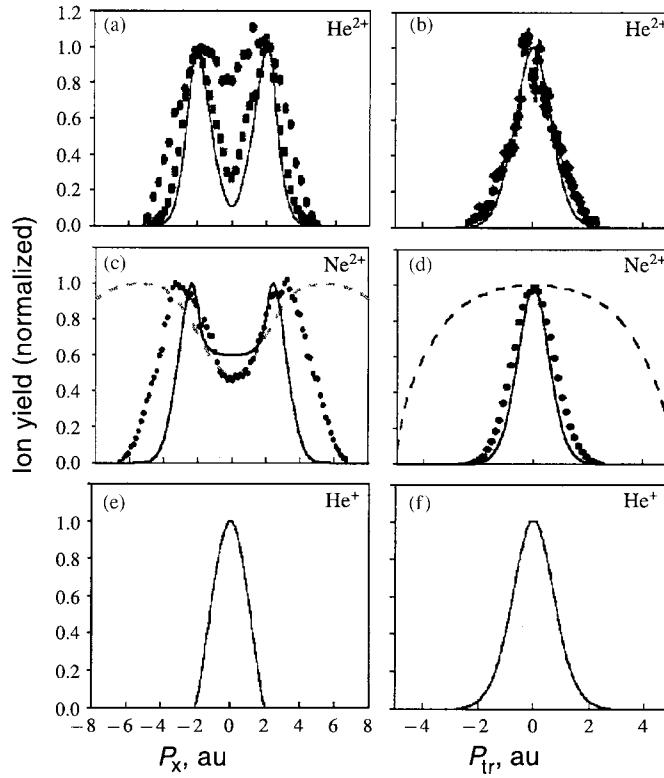
Figure 13. Comparison of theory and experiment for the distributions of the recoil momentum: He^{2+} ions (a) parallel and (b) perpendicular to the polarization axis; experimental data (circles, [211]), full S-matrix calculation (squares, [13]) and the calculated results obtained using a stationary-phase approximation (lines, [174]); $\lambda = 780$ nm and $I = 6.6 \times 10^{14}$ W cm^{-2}. Also shown are the results of S-matrix calculations within the stationary-phase approximation only (lines, [174]): panels (c) and (d) at 800 nm and 1.3×10^{15} W cm^{-2} for Ne^{2+}; experimental data (circles, [144]). Additional calculations using stationary-phase approximation: Panels (e) and (f) at 780 nm and 6.6×10^{14} W cm^{-2} for He$^+$(2s) (from [174], reproduced with permission of the authors).

the He^{2+} recoil momentum, $\mathbf{P}$, satisfies $\mathbf{P} = -(\mathbf{k}_a + \mathbf{k}_b)$; the photon momentum itself is negligible (long wavelength approximation). It is seen from figure 13 that the results of the full calculations (squares, [13]) as well as those using the stationary-phase approximation (line, [174]) compare well with the experimental data. The presence of the double hump in the parallel direction, panel (a), and the single hump in the perpendicular direction, panel (b), is well reproduced. The width of the experimental distributions and the positions of the maxima are also reproduced by the calculations. There is a difference, however, for the central minimum in the distribution of the parallel momentum component (panel a), which might be due to non-negligible contributions from diagrams in the higher order terms of the S-matrix expansion (see also discussion in subsection 5.4). We note that in the case of Ne^{2+} calculations have been performed so far using the additional stationary-phase approximation [174] of the CES amplitude, and again an overall agreement between the calculation and the experimental data [144] is found. It may be noted that for the parallel distributions the observed minimum in panel (c) seems to be better reproduced than that in panel (a), while the width is less well reproduced. For the perpendicular distribution in panel (d), the theoretical result (solid line)
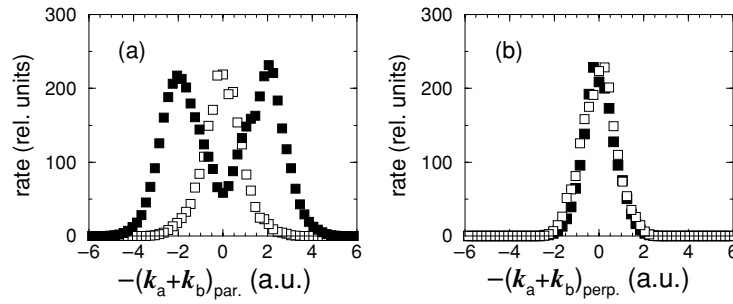
Figure 14. Distributions of the recoil momentum of He^{2+} ions: (a) parallel and (b) perpendicular to the polarization axis. Comparison of IMST calculations of the CES diagram (cf [13]) *with* the final-state Volkov dressing of the two outgoing electrons (filled squares) and calculations *without* the final-state Volkov dressing (open squares). Laser parameters: $\lambda = 800$ nm, $I = 6.6 \times 10^{14}$ W cm^{-2}. The results show the importance of the effect of dressing of the final-state electrons by the field and the origin of the observed double-hump parallel distribution.

agrees well with the observation. The dashed line corresponds to a model with a *constant* $e − 2e$ rate, which, however, is quite unphysical.

The experimental and the theoretical distributions parallel to the field direction (cf figure 13(a)) show the characteristic double-hump structure with a central minimum. The origin of this structure has been analysed by Becker and Faisal [13]. It has been found to be due to the combined effect of electron–electron correlation *and* final-state Volkov dressing of the two outgoing electrons. Thus, it can be seen from figure 14, where results of calculation for the parallel distribution (a), and the perpendicular distribution (b), are presented. The distributions *with* the Volkov dressing in the final state (filled squares) and *without* the Volkov dressing (open squares) are compared. One sees that the wide two-hump distribution parallel to the polarization direction collapses into a narrow single-hump distribution in the *absence* of the final-state Volkov dressing (panel a). This clearly shows the critical importance of the final-state field effect for the two-hump momentum distribution. On the other hand, the distribution perpendicular to the field direction does not essentially change (panel b); this can be physically understood from the fact that the final-state momenta of the outgoing electrons do not couple to the field significantly perpendicular to the field polarization, in that direction the classical force exerted on the electrons by the field is zero. We may note here parenthetically that such comparisons, while difficult to implement in numerical wavepacket simulations, can be readily made within the IMST. In fact, the distributions without the Volkov dressing in the final state are calculated by simply replacing, in equation (79), the two-electron Volkov wavefunction in the final state by two plane waves of the respective momenta.

It has been further shown by Jaroń and Becker [92] that the component of the sum-momentum parallel to the field is the largest, when the drift energy of the active electron in the intermediate state is close to zero. This is due to the fact that the additional energy transfer from the field is most probable, when the momentum transfer is large. The maximum of the distribution at the present laser parameters is produced by intermediate-state Volkov electrons with energies well below the magnitude of the binding energy of He^+. Therefore, the second step of the CES mechanism can be thought of as an *internal* laser-induced inelastic scattering (rescattering) process.

Calculations, for He atom, of the direct coincidence distributions for the momenta of the two electrons, parallel to the field direction, reveal a maximum probability for the emission of the electrons in the *same* half-plane, and for equal *but* non-zero values [18]. This prediction is consistent with the main feature of the experimental observations (for Ar and Ne atoms)
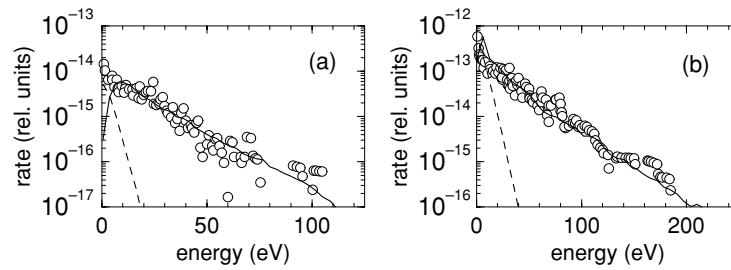
Figure 15. Electron energy distributions from double ionization of He, theoretical results (cf [18]) from the rescattering diagram (solid lines) are compared with those of the shake-off diagram (dashed lines) and experimental results (circles, [120]).

reported by Weber *et al* [212, 213] and Feuerstein *et al* [72]. Interestingly, in the experiments additional weaker but significant probabilities have been observed also in the second and the fourth quadrant. They go beyond the first-order effect of the electron–electron correlation considered so far in the CES diagram (cf further discussion in section 5.4).

Another important test of the rescattering (CES) mechanism was provided by the measurement of the coincidence distribution of the *energies* of the two electrons in the double ionization process by Lafon *et al* [120]. The results of the IMST calculations from the CES and the SO diagrams of the coincidence energy distributions are reproduced in figure 15 and compared [18] with these data. In the experiment (and in the calculations) one electron of a given energy has been observed along the polarization direction in coincidence with the other electron whose energy and emission direction, however, were kept unresolved (integrated). Since the experimental counts had been given in an arbitrary scale, for this comparison the theoretical predictions for the two mechanisms had been matched with the data at one energy[8]. It can be seen from the figure that the experimental data (circles) are reproduced remarkably well by the theoretical results obtained from the CES diagram (solid lines). Especially, the slow decrease of the signal with increase of the electron energy is significant. In a narrow region near the threshold there is a difference between the calculated and the experimental results, which suggest possible contributions of additional processes (cf next subsection) in the threshold region. In sharp contrast to the CES mechanism, the distributions from the SO diagram (dashed line) decrease very rapidly within a few tens of eVs and fail completely to follow the trend of the experimental data. This comparison between theory and experiment, therefore, completely rules out the SO mechanism in favour of the rescattering (CES) mechanism, for the non-sequential double ionization process (in the laser parameter domain of the experiment).

5.4. Higher order terms

The above comparison suggests that contributions from higher order effects might be necessary to account for certain features observed in the coincidence distributions. For example, at the next leading term (third order) of the IMST expansion, a diagram, presented in figure 16, shows up, which implies an excitation of the He^+ ion by the active electron via the electron–electron correlation, followed by ionization of the excited state by the laser field. Intuitive proposals of this effect have been made recently to extend the heuristic rescattering models [29, 72, 220].

---

[8] Note that due to this matching the predictions from the SO and the CES diagrams are shown on a *relative* scale. As shown in figure 12(a), there is a large difference in the *absolute* magnitude between the predictions of the two mechanisms.
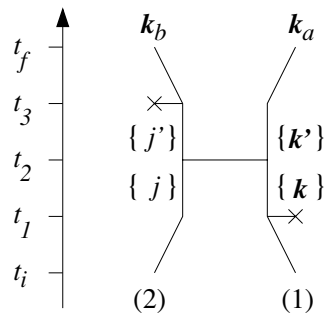
Figure 16. Third-order diagram for double ionization of a two-electron atom.

For example, the intermediate excitation mechanism could break the temporal correlation between the emission of the two electrons, which might then result in contributions in the second and fourth quadrant in the coincidence distributions of the momentum components parallel to the field direction. This could give further contribution and raise the minimum of the double-hump distribution of the recoil-ion discussed above. In general, the third-order diagram in figure 16 is rather difficult to evaluate exactly with actual Coulomb interactions included. However, an estimate of the diagram has been made for recoil-ion momentum distribution by Kopold *et al* [108] using the stationary-phase approximation and replacing the Coulomb interaction by the zero-range contact potential. It was found that its main contribution appears near the zero of the recoil-ion momentum where in fact the (second-order) CES diagram was found to underestimate the experimental data (cf figure 14). However, no satisfactory conclusion regarding this problem could be made with available information yet. Another effect of the excitation mechanism could be to provide additional slow electrons that may help to fill the gap between theory and observation, *close* to the threshold, for the coincidence energy distributions discussed above (see figure 15). However, this has not yet been demonstrated to be the case or not.

The apparent importance of the role of inter-electron correlation in the non-sequential double ionization raises the question if a description of the interaction in the first order only (as in the CES diagram) is sufficient. This could be best tested by considering the perpendicular components of the momentum distributions since as discussed above these components are hardly affected by the presence of the field and therefore should reflect the influence of the three-body Coulomb interaction most directly. To this end the CES (rescattering) diagram can be extended to the corresponding diagram that includes the electron–electron interaction to *all* orders in the final state. The full electron–electron interaction is indicated by the dashed line connecting the electrons at $t = t_f$ in the extended CES diagram, figure 17(a).

To answer the question raised above, Weckenbrock *et al* [215] have measured experimentally the perpendicular coincidence distributions in greater details. The experimental results are shown in figure 17(b) (left-hand panel) in which the coincidence distribution of the momentum components k_{xeb} and k_{yeb}, of one of the electrons (*b*) in the plane perpendicular to the polarization axis, and the momentum component k_{ea} of the other electron in the *same* plane (indicated by the arrow) are plotted and compared with the corresponding theoretical results obtained from the simple CES (right-hand panel) and the extended CES diagrams (middle panel). For the calculations of the extended CES diagram, the *exact* solution derived by Faisal [64, 8] of the Schrödinger equation of two Coulomb-interacting electrons subjected to the laser field has been used in the final state. The analytical expression of the extended
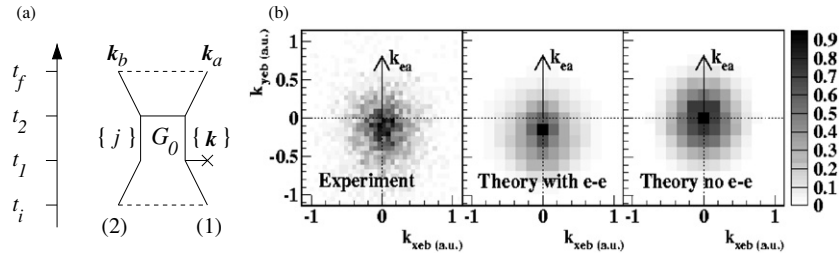
Figure 17. (a) An extended CES diagram including the electron–electron interaction to all orders in the final state. (b) Coincidence distributions of electron momenta of one electron, k_{xeb} and k_{yeb}, perpendicular to the polarization axis and the momentum k_{ea} of the other electron in the same plane. Experimental distributions (left-hand panel), are compared with the theoretical results calculated with the full electron–electron correlation in the final state (middle panel) and those neglecting the full final-state correlation (right-hand panel) (from [215]. Copyright 2003 by the American Physical Society).

CES amplitude is then evaluated using a similar procedure to that used by Becker and Faisal for the computation of the simple CES amplitude (cf equation (79)) discussed earlier. The experimental and theoretical data are integrated over the parallel components and over the magnitude of momentum of the other electron a.

The experimental data (figure 17(b), left-hand panel) clearly show that the two electrons are emitted preferentially back-to-back, indicating a strong Coulomb interaction between the electrons. As can be seen in the middle panel of figure 17(b), the theoretical results from the extended CES diagram reproduce the experimental data well, while those neglecting the electron–electron interaction in the final state (right-hand panel) do not show the back-to-back characteristic. Thus, we conclude that the extended CES diagram that goes beyond the simple CES diagram provides an explanation of the observed back-to-back emission (in the plane perpendicular to the polarization axis) and, hence, confirms the importance of the full electron–electron repulsion in the final state for the non-sequential double ionization process.

Indications of the influence of the final-state correlation on the parallel distributions, in a case when the transverse component of at least one of the electrons is small, have been found recently by Figueira de Morisson Faria *et al* [74, 75]. We may note that this analysis has been made using the stationary-phase approximation and assuming the zero-range interaction potential in place of the actual Coulomb interaction.

5.5. Ion yields in double, multiple and inner-shell ionization

Total ion yields from double ionization of the noble gas atoms, He, Ne, Ar, Kr and Xe, as well as the ratios of the double-to-single ionization in these atoms, as a function of the laser intensity, have been measured extensively (e.g. [76, 104, 208, 83, 121]). Moreover, threefold ionization of argon [121], up to fourfold ionization of Kr [124, 49], up to sixfold ionization of Xe [121] and (most recently) up to twentyfold ionization yields of Xe [219] have also been observed. These ion yield signals range dynamically over many orders in magnitude while the intensities range from about 10^{13} W cm^{-2} to about 10^{16} W cm^{-2}.

Ab initio quantitative analysis of these experimental data, in particular for atoms other than the He atom, poses a formidable problem. We indicated earlier that IMST can help in constructing simple models by suggesting appropriate places for introduction of physical hypothesis to gain insights into complex situations that may be otherwise unaccessible to the *ab initio* analysis. In order to analyse these data, therefore, a simple model for estimating
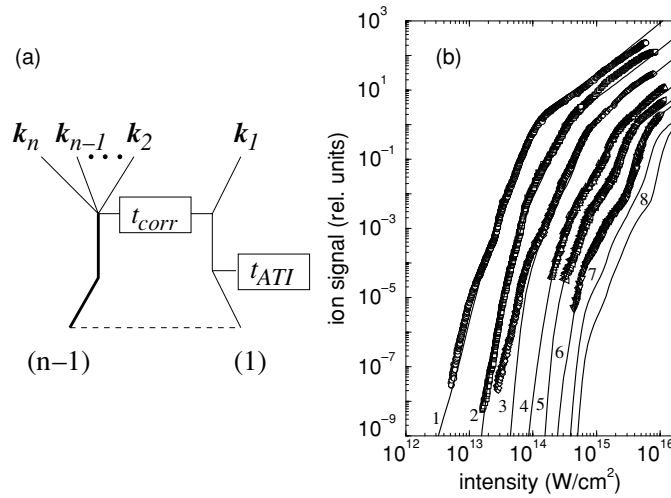
Figure 18. (a) Diagram for laser-induced non-sequential n-fold ionization. The lines stand for the evolution of the states of the atomic electrons in time. t_{ATI} is the T-matrix for a virtual ATI-like transition and t_{corr} is the T-matrix for the e–ne transition. (b) Comparison between experimental data [121] and theoretical model predictions (cf [11]) for n-fold ionization ($n = 1$–8) in Xe atom at $\lambda = 800$ nm and $\tau = 200$ fs.

the total ionization rate of laser-induced non-sequential double *and* multiple ionization of complex atoms has been proposed by Becker and Faisal [10, 11]. The model is suggested by the dominant correlated energy-sharing diagram for double ionization of He. As discussed already, in a first stage an active electron absorbs the field energy and shares it with the other electron by Coulomb interaction which can lead to the emission of both the electrons. Physically, the first stage is analogous to the ATI process in single ionization and the second stage is equivalent to an (e⁻, 2e⁻) collisional–ionization by the internally produced ATI electrons. This suggests that a possible physical mechanism for the n-fold multiple ionization could be given by a diagram analogous to the two-electron CES diagram in which the first stage of the production of an energetic electron by ATI mechanism remains the same, but the second stage would be the generalization of the (e⁻, 2e⁻) collision–ionization (for double ionization) into an (e⁻, ne⁻) collision–ionization in the multiple ionization case. The corresponding generalized Feynman-like diagram for the laser induced non-sequential *multiple* ionization is shown in figure 18(a) according to which at first one electron (say, '1') absorbs the field energy by the above-threshold ionization process and propagates with momentum k in the Volkov state while the other electrons propagate in the virtual states of the ion. Then, the active electron couples to the $(n - 1)$ other electrons by electron–electron correlation V_c (i.e. (e⁻, ne⁻) collision) to all orders, until the n electrons escape together.

An exact evaluation of the diagram, including all orders of the ATI and the correlation interaction, is practically impossible for a large value of n. An approximate estimate of the total rate, however, can be obtained in terms of a model rate formula constructed as the product of the rate of the first-stage ATI process combined with the rate of the second-stage (e⁻, ne⁻) process, for each value of the total number of photon absorbed, and summed over all values of the intermediate numbers of absorbed photons for the ATI electron weighted by the density of intermediate momentum states at the ATI momenta, k_N. Thus, the model formula for the

total rate of n-fold multiple ionization of a many-electron atom, from a given initial electron configuration i to a final ion configuration f, is given by [11]

$$\Gamma_i^{n+} = \sum_f P_{fi} \Gamma_{fi}^{(ne)}. \tag{80}$$

$\Gamma_{fi}^{(ne)}$ is the non-sequential rate for the direct emission of n electrons from the configuration i into the final ionic configuration f, which linearly combines the products of the two individual processes,

$$\Gamma_{fi}^{(ne)} = \sum_{N=N_0}^{\infty} \sum_j \Gamma_{f,j}^{(e,ne)}(\mathcal{E}_N) \frac{\pi k_N}{2} \Gamma_{j,i}^{(ATI)}(\boldsymbol{k}_N \| \boldsymbol{\epsilon}), \tag{81}$$

where, $\Gamma_{j,i}^{(ATI)}(\boldsymbol{k}_N \| \boldsymbol{\epsilon})$ is the differential ATI rate per electron for absorption of N photons from the field and $\Gamma_{f,j}^{(e,ne)}(\mathcal{E}_N)$ is the (e^-, ne^-) rate, which is evaluated here at the 'incident' energy $\mathcal{E}_N = k_N^2/2 + 4k_N\sqrt{U_p} + 8U_p$ with $k_N^2/2 = N\omega - U_p - E_B$. This incident energy is assumed to be the maximum classical energy attainable in the field. The combinatoric factor

$$P_{fi} = \prod_s \binom{n_i^s}{n_f^s} \tag{82}$$

is the number of ways the n electrons can be ejected from the initial occupied configuration i into the final configuration f; n_i^s and n_f^s are the number of electrons in the sth sub-shell of the initial and final configurations, respectively. For the computations of the individual ATI rates the Coulomb corrected KFR formulae is used, as discussed above (equation (50)), and for the computation of the (e^-, ne^-) collisional ionization rates the simple formulae due to Lotz [128] for the $(e^-, 2e^-)$-processes, and due to Fisher *et al* [77] for the (e^-, ne^-)-processes ($n > 2$), have been used.

In order to compare with the experimental ion yields, the predictions of the model formula for n-fold ionization rates (as well as the sequential single ionization rates) have been used to get the ion yields as a function of the laser intensity. The latter have been constructed using the model rates in the corresponding *system* of *rate equations* that couple the yields of the various charge states with one another. The model results when compared with the data are found to give good agreement with the experimental data in virtually all cases considered [10, 11, 67, 12, 129]. Thus the observed yields of double ionization, as well as the ratios of double-to-single ionization, of the sequence of noble gas atoms He, Ne, Ar, Kr and Xe are reproduced remarkably well except for the Ne atom [12]. It should be recalled here that in the data for the recoil-ion momentum distributions of He, Ne and Ar, a similar qualitative difference for the Ne atom, compared to those for the He and Ar atoms, has also been observed [146]. The origin of this 'Ne anomaly' is not understood at present.

The predictions of the above model are also in good agreement with the experimental yields of *multiple* ionization up to Ar^{3+} [121], Kr^{4+} [49] and Xe^{6+} [121]. As an example, in figure 18(b) the comparison for the case of the n-fold ionization ($n = 1 - 8$) of Xe with the experimental data, obtained by Larochelle *et al* [121], is shown.

We may note further that the agreement of the model results with experimental data includes the much discussed *knee* structure in the NSDI experiment (e.g. Walker *et al* [208]) for the non-sequential double ionization of He atom; the model in fact reproduces the intensity dependence of the observed data over the entire dynamical range of *twelve orders* of magnitude in the ion signal for the near infrared wavelengths; the knee structure is found there to arise from a competition between the NS mechanism and the saturation effect for the ionization process involved. It should be noted further that the model is also consistent with the *absence*
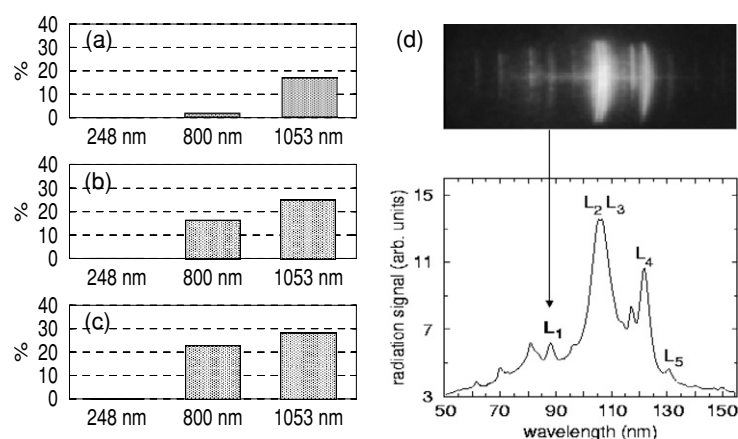
Figure 19. Percentage of Ar^{2+} ions having an inner-shell vacancy in the 3s shell for three wavelengths at different laser peak intensities: (a) $I = 4 \times 10^{13}$ W cm^{-2}, (b) $I = 7 \times 10^{13}$ W cm^{-2}, (c) $I = 1 \times 10^{14}$ W cm^{-2}. (d) Radiation spectrum of Ar at 1053 nm and 600 fs as a function of the wavelength. The line L1 corresponds to the inner-shell transition in Ar^{2+} (cf [12]).

of the knee-structure at the UV wavelength (e.g. in the experiment by Charalambidis *et al* [33]; cf solid lines in figure 10).

Inner-shell ionization in an intense laser field is a new problem that has not been investigated as extensive as double or multiple ionization. The first of such investigations, however, has recently began. Thus, it has been predicted theoretically by Becker and Faisal and confirmed experimentally by Chin and collaborators [14] that even in a near-infrared laser field, electrons from the *inner* shells can be ejected through the mechanism of non-sequential double and multiple ionization. Calculations based on the model formula, equation (81), have been performed for Ar atoms at different wavelengths and intensities. In figures 19(a)–(c) the percentage of Ar^{2+} ions, found in the [Ne]$3s3p^5$ configuration with a vacancy in the 3s shell, are presented. It can be seen from the results that at the longer wavelengths a percentage up to as much as 30% of the total number of Ar^{2+} ions can occur with a hole in the 3s shell due to a non-sequential double ionization process. Consistent with this, at a shorter wavelength ($\lambda = 248$ nm) the Ar^{2+}([Ne]$3s3p^5$) yield is found to be negligible, since the laser-induced double ionization at 248 nm is entirely governed by the sequential double ionization process, as discussed above. The creation of the predicted 'hollow ion' has been experimentally confirmed as follows. A hole in the 3s shell of the doubly ionized Ar atom can only be subsequently filled by a 3p electron under emission of fluorescence radiation, since the energy of the excited state is too small for an Auger transition. The fluorescence spectra of argon, measured by Chin and co-workers [14] using an intense Ti:sapphire/Nd:glass laser operating at $\lambda = 1053$ nm, are shown in figure 19(d). The line L1 agrees with the known wavelengths of the six strong lines between 87.1 nm and 88.7 nm associated with the fluorescence emission due to the radiative filling of the 3s vacancy in doubly ionized Ar (in closely lying different quantum numbers J). Due to the finite resolution of the experimental set-up, the six closely lying lines could not be separated individually in the experiment.

6. Ionization of molecules in intense fields

Interaction of molecules with an intense laser pulse has generated much experimental and theoretical interest in the recent years (for reviews, see e.g. [6, 176, 177]). It is particularly

interesting because of the extra degrees of freedom, like rotation and vibration of the nuclear frame, that are obviously absent in the atomic case. A variety of intense-field processes have been observed for molecules, including single and multiple ionization and harmonic generation, which are analogues of the processes in atoms. Dissociative ionization, Coulomb explosion, fragmentation and simultaneous fragmentation/ionization with molecular alignment, ionization with vibrational excitation etc are also being observed in the molecular case.

Single ionization of molecules is perhaps the most fundamental process among them as it often occurs as a precursor of most of the other reaction processes. Calculations based on the single-active-electron approximation, like in the case of atoms, have been very successful in predicting ionization yields, ATI spectra and HHG spectra of simple one- and two-electron molecules. *Ab initio* numerical simulations have been performed for H_2^+, H_2 and H_3^+ (e.g. [87, 7]). They are extremely difficult to carry out for more than two electron systems and are not possible for larger molecules with any currently available computing machines. As in the atomic case, the IMST offers an *ab initio* systematic approximation method of investigation which can partially go round this obstacle and study the response of many-electron diatomic (and even polyatomic) molecules to an intense laser field.

Thus, the IMST has been extended by Muth–Böhm *et al* [151, 152] to calculate the ion yields from the outer and inner valence shells of a diatomic and polyatomic molecules. One of the interesting results of these investigations has been the identification of the signature of the molecular orbital symmetry and the molecular alignment in the angular (and energy) distributions of the photo-electron, as well as in the total ion yields. Below we briefly discuss the extension of the IMST to the case of single ionization of a polyatomic molecule. The expression for the differential and total ionization rate formula are given *and* the theoretical ion yields for a number of specific cases are discussed and compared with the experimental observations.

6.1. Rate of ionization of diatomic and polyatomic molecules

Using the lowest order IMST, the rate of ionization of a polyatomic molecule has been derived by Muth–Böhm *et al* [151, 152]. The corresponding diagram is completely analogous to that considered for the atomic case (cf figure 1(a)) The associated ionization amplitude involves a transition matrix element between the unperturbed initial bound state of the molecule, Φ_i, and the final product state of the Volkov state of the free electron and the unperturbed bound state of the residual molecular ion, Φ_f. This in fact is a direct analogue in the molecular case of the well-known KFR formula of the atomic case. The associated doubly differential ionization rate, from a molecular state with N_e electrons and subjected to a linearly polarized laser field, is given by [151, 152]:

$$\frac{\mathrm{d}W_{fi}^{(N)}(I, \hat{\boldsymbol{n}})}{\mathrm{d}\Omega} = 2\pi N_e C_{\mathrm{coul}} k_N (U_p - N\omega)^2 J_N^2 \left(\boldsymbol{\alpha}_0 \cdot \boldsymbol{k}_N, \frac{U_p}{2\omega} \right)$$
$$\times |\langle \phi_{\boldsymbol{k}_N}(\boldsymbol{r}_1) \Phi_f^+(\boldsymbol{r}_2, \ldots, \boldsymbol{r}_n) | \Phi_i(\boldsymbol{r}_1, \ldots, \boldsymbol{r}_n) \rangle (\hat{\boldsymbol{n}})|^2, \tag{83}$$

where N is the number of absorbed photons. Dependence of the rate of ionization on the *orientation* of the molecular axes in space is determined in equation (83) via the unit vector $\hat{\boldsymbol{n}}$. Hence, any distribution of molecular axis in an ensemble of randomly oriented molecules can be taken into account by averaging the rates over the angles $(\theta_{\hat{\boldsymbol{n}}}, \phi_{\hat{\boldsymbol{n}}})$. By summation over the number of photons N one can readily obtain the photoelectron energy distribution (ATI spectra) in any particular direction of ejection of the electron. Similarly the total ionization rate is obtained by further integrations with respect to the ejection angles of $\hat{\boldsymbol{k}}_N$. As before,

(a) N$_2$ (b) O$_2$
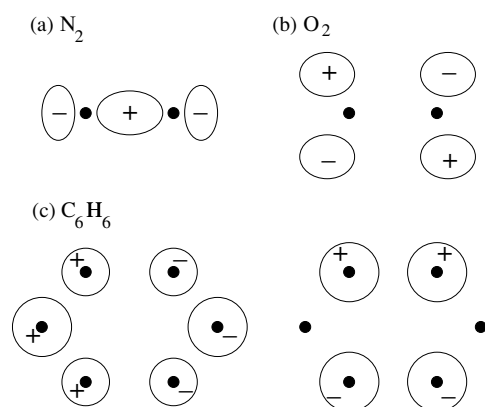
(c) C$_6$H$_6$

Figure 20. Schematic presentation of the highest occupied molecular orbitals (HOMOs) of (a) N$_2$(σ_g, bonding orbital), (b) O$_2$(π_g, anti-bonding orbital) and (c) C$_6$H$_6$(e_{1g} orbitals, pairs of anti-bonding symmetry). Note that for C$_6$H$_6$ only the shape and the sign of the functions above the C$_6$ plane are shown.

a comparison with experiment is possible at present only at the level of the measured ion yields. They can be constructed theoretically from the basic rates of ionization, equation (83), combined with the rate equations of the neutral and ionized populations [94], in the same way as discussed above for the atomic case.

For theoretical analysis and intuitive interpretation of the results, it is quite useful to express a molecular orbital as a linear combination of atomic orbitals:

$$\Phi(\boldsymbol{r}; \boldsymbol{R}_1, \boldsymbol{R}_2, \ldots, \boldsymbol{R}_n) = \sum_{i=1}^{n} \sum_{j=1}^{j_{\max}^{(i)}} a_{i,j} \phi_{i,j}(\boldsymbol{r}, \boldsymbol{R}_i), \tag{84}$$

where $\phi_{i,j}$ are the atomic orbitals with the coefficients $a_{i,j}$, $j_{\max}^{(i)}$ is the number of atomic orbitals and $\boldsymbol{R}_i$ are the positions of the ith nucleus in the molecule. The atomic orbital coefficients can be obtained using quantum chemical codes, such as the GAMESS code [191]. The above form of the molecular orbital can be rewritten in the case of a symmetric di- or polyatomic molecule, consisting of p homonuclear pairs of atoms, as

$$\Phi(\boldsymbol{r}; \boldsymbol{R}_1, \boldsymbol{R}_2, \ldots, \boldsymbol{R}_{2p}) = \sum_{i=1}^{p} \sum_{j=1}^{j_{\max}^{(i)}} a_{i,j} \phi_j(\boldsymbol{r}, -\boldsymbol{R}_i/2) + b_{i,j} \phi_j(\boldsymbol{r}, \boldsymbol{R}_i/2). \tag{85}$$

Thus, any molecular orbital of a complex symmetric molecule could be considered as a *sum* of p pairs of orbitals of the effective homonuclear 'diatomic molecules'. For a symmetric molecule the p homonuclear pairs of orbitals have either all *bonding*-like or all *anti-bonding*-like symmetry[9]. To illustrate this, in figure 20 the schematic shapes of the highest occupied molecular orbitals of three selected molecules are shown: (a) N$_2$(σ_g, bonding symmetry), (b) O$_2$(π_g, anti-bonding symmetry) and (c) C$_6$H$_6$(e_{1g}, pairs of anti-bonding symmetry). Note, that for a bonding molecular orbital pair the atomic orbital coefficients have the same value and sign, i.e. $a_{i,j} = b_{i,j}$, while, in contrast, for an orbital pair with anti-bonding symmetry one has $a_{i,j} = -b_{i,j}$. For non-symmetric molecules they are in general different.

[9] The nomenclature 'bonding' and 'anti-bonding' symmetry refers in the present context to each pair of identical atoms only, and not to the symmetry of the whole molecular orbital.

Before proceeding to discuss a number of applications of the IMST in the molecular case, we note that a tunneling rate formula based on an extension of the ADK model for atoms [4] to diatomic molecules has been given by Tong *et al* [204, 221] recently. We may point out that the first-order term of the IMST series in the Keldysh tunnel-limit $\gamma = F^2/4\omega^2 \ll 1$ automatically leads to a tunnel formula analogous to the atomic case discussed above. The relation between the molecular case and the atomic case becomes particularly clear if the LCAO-molecular orbitals are first re-expressed as a single-centre expansion (e.g. [86, 52]) about the centre of the charge distribution of the molecule.

6.2. Suppressed molecular ionization

Early measurements of ion yields of diatomic molecules by CO_2 lasers by Gibson *et al* [80] and Chin and coworkers [35, 209, 210] indicated that the ionization yields were nearly identical to those of atoms having comparable ionization potentials, such atoms are conveniently referred to as 'companion atoms' [151, 152]. This similarity of the ionization yields of a molecule and its companion atom has been thought to be a consequence of the 'tunneling ionization' in intense infrared and near infrared wavelengths, in which the ionization probability primarily depends on the ionization potential and the field strength. More recent works using Ti:sapphire laser systems, however, have shown that the ionization yield of O_2 [201, 83] is suppressed, contrary to expectation, by more than an order of magnitude compared to that of its companion Xe atom, while the ionization signal of N_2 remained comparable, as expected, to that of its companion Ar atom. Furthermore, a study of a large number of organic molecules showed [84, 85] that all these molecules were considerably harder to ionize than the companion rare gas atoms.

This phenomenon, called suppressed molecular ionization, had been analysed theoretically first by Muth-Böhm *et al* [151, 152] using the first-order IMST. The total rate of ionization for a symmetric molecule with N_e equivalent electrons in the highest occupied molecular orbital (HOMO or valence orbital), with p bonding, or anti-bonding, pairs of atomic orbitals, equation (83), reduces to

$$\Gamma_{\text{mol}}^+ = N_e \sum_{N=N_0}^{\infty} \int d\hat{\boldsymbol{k}}_N \frac{dW(\boldsymbol{k}_N)}{d\hat{\boldsymbol{k}}_N} \tag{86}$$

with the differential ionization rate given by

$$\frac{dW(\boldsymbol{k}_N)}{d\hat{\boldsymbol{k}}_N} = 2\pi C^2(Z, E_B, F) k_N (U_p - N\omega)^2 J_N^2\left(\boldsymbol{\alpha}_0 \cdot \boldsymbol{k}_N, \frac{U_p}{2\omega}\right)$$

$$\times \left|\sum_{j=1}^{p} \langle \phi_{\boldsymbol{k}_N}(\boldsymbol{r}) | \tilde{\phi}_j(\boldsymbol{r}) \rangle \begin{cases} \cos(\boldsymbol{k}_N) \cdot \boldsymbol{R}_j/2) \\ \sin(\boldsymbol{k}_N) \cdot \boldsymbol{R}_j/2) \end{cases}\right|^2 \begin{array}{l} : \text{bonding orbital pairs} \\ : \text{anti-bonding orbital pairs,} \end{array} \tag{87}$$

where

$$\tilde{\phi}_j(\boldsymbol{r}) = 2 \sum_{i=1}^{i_{\max}^{(j)}} a_{i,j} \phi_{i,j}(\boldsymbol{r}). $$

According to equation (87) the differential rate of ionization of a symmetric molecule by any N number of photon absorption consists essentially of two major parts, namely an atom-like part that depends on the atomic orbitals as well as their coefficients appearing in the active molecular orbital of interest (HOMO), and a trigonometric part
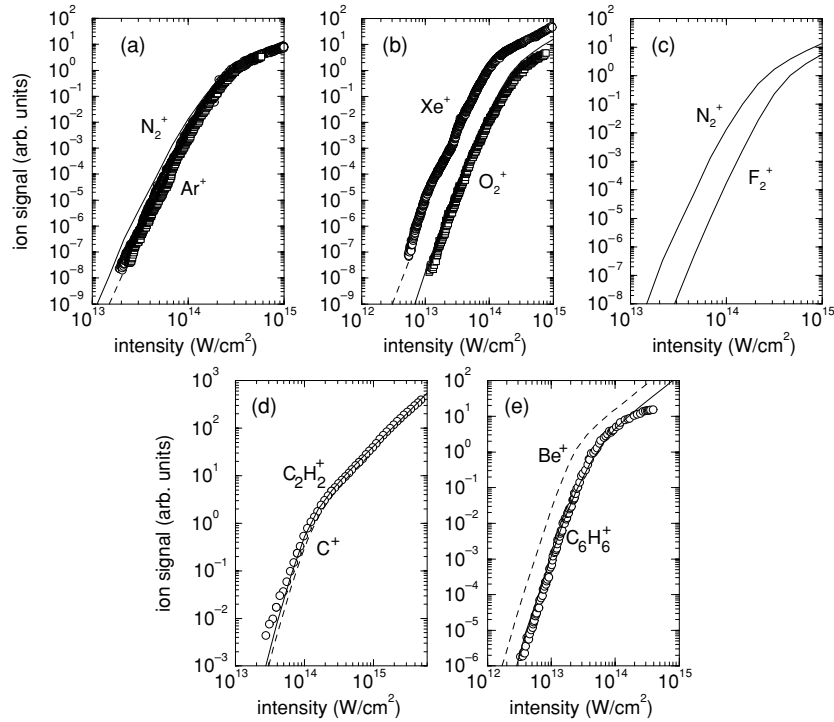
Figure 21. Comparison of the predictions of the Coulomb-corrected KFR model (lines, cf [151, 152]) for the ion yields of atoms, di- and polyatomic molecules among each other and with experimental results: (a) N_2 and Ar, $\lambda = 800$ nm, $\tau = 200$ fs [201]; (b) O_2 and Xe, $\lambda = 800$ nm, $\tau = 200$ fs [201]; (c) N_2 and F_2, $\lambda = 800$ nm, $\tau = 200$ fs; (d) $C_2 H_2$ and C, $\lambda = 800$ nm, $\tau = 50$ fs [39]; (e) $C_6 H_6$ and Be, $\lambda = 800$ nm, $\tau = 200$ fs [203]. Results obtained for the molecules are given by solid lines (theory) and circles (experiment), while those for the companion atoms are marked by dashed lines (theory) and squares (experiment).

depending on the structure of the nuclear frame. The latter is seen to be associated with *interference* effects between the waves of the ionizing electron centred about the individual atoms (or atom pairs). In general, these interference effects would tend to behave destructively for molecules having a valence orbital consisting of *anti-bonding* orbital pairs, but *not* for the bonding orbital pairs. This is because for small values of the arguments of the sinusoidal factors (for small k_N or the first few and dominant photon orders N) $\sin(\mathbf{k} \cdot \mathbf{R}_j/2) \ll 1$ and $\cos(\mathbf{k} \cdot \mathbf{R}_j/2) \approx 1$. One may also expect that the interference effects would be most effective for symmetric polyatomic molecules with small internuclear separation between the atoms of the pair, but would tend to decrease for larger molecules with increasing separations between the atom pairs. Equation (87) shows that the ionization rate of a molecule tends to be bounded from above by that of a single centred effective atomic system with the same ionization potential as of the molecule; this appears to be consistent with the ionization of a large number of complex molecules as in the experiments by Hankin *et al* [84, 85], where the saturation intensities have been found all to lie *above* the saturation intensities of the corresponding companion atoms.

In figure 21, we compare the theoretical results for the ion yields of a number of diatomic [151, 17] and polyatomic [152] molecules and their companion atoms with the experimental observations [201, 39, 203]:

(a) Ar (binding energy: 15.76 eV) and N_2 (bonding pair, 15.58 eV),
(b) Xe (12.13 eV) and O_2 (anti-bonding pair, 12.07 eV),
(c) N_2 and F_2 (anti-bonding pair, 15.69 eV),
(d) C (11.26 eV) and $C_2 H_2$ (bonding pairs, 11.40 eV),
(e) Be (9.32 eV) and $C_6 H_6$ (anti-bonding pairs, 9.26 eV).

It can be seen that the ion yields of the molecules that have a HOMO with atomic orbital pairs of anti-bonding symmetry are strongly reduced compared to those of their companion atoms. In contrast, molecules with their active molecular orbital consisting of atomic orbital pairs of bonding symmetry do not show such a large reduction. This is in agreement with the interpretation of the molecular symmetry and the destructive versus constructive interference effects, discussed above. We may point out here parenthetically that if instead of the LCAO-MO representation of a multi-centre molecular orbital, one expresses it as a mathematically equivalent *single* centre MO [51, 52, 86], then there is obviously a single-centre wave (that arises from the common mathematical centre of the molecule) and one loses the 'physical picture' of interference of the waves arising from the different *atomic* centres.

The calculated ion yields of these molecules agree well with the respective experimental data in all cases examined so far but one. The exceptional case has been found by Jones and coworkers [43, 217] for the molecule F_2. Although it has a valence orbital with an anti-bonding symmetry, it does *not* show a suppression of ionization compared to its companion Ar atom. It is not at present clear what the origin of this 'F_2 anomaly' is. We should note here that the use of the Hartree–Fock molecular orbitals in these calculations turns out to be particularly poor for the F_2 molecule (a 'HF-sick molecule'). It is not unlikely, therefore, that correlation would play a role in explaining this discrepancy. If so, it would be interesting to find out whether the static ground-state correlation or a dynamic correlation effect (that acts in the intermediate and/or the final state in conjuction with the field) would lead to a clarification of the situation.

Signatures of the interference effects, predicted by the *S*-matrix theory, at a deeper level than that of the total ion yield have been seen recently in the ATI spectra of the diatomics N_2 and O_2 and its companion atoms Ar and Xe by Grasbon *et al* [82]. Thus, the lowest order ATI peaks of O_2 are reduced compared to that of its companion atom Xe as predicted by the theory. Furthermore, with increasing energy the peaks in the ATI spectra of the oxygen molecule were seen to approach from below those of Xe, and the peaks for N_2 remained comparable to that of its companion Ar atom, over the whole energy range. These qualitative observations are again consistent with the expectations based on the calculations [82].

In this context we may further note that the interference mechanism as expressed in the rate formula, equation (87), suggests that the energy spectra of homonuclear diatomic molecules may be also 'suppressed' not only near the threshold but also at certain *higher* energy values. They are given by [94, 95]:

$$\frac{k_N^2}{2} = \frac{2}{R^2(\hat{k}_N \cdot \hat{n})^2} \begin{cases} n^2\pi^2 & \text{for anti-bonding symmetry} \\ n^2\pi^2/4 & \text{for bonding symmetry,} \end{cases} \tag{88}$$

with $n = 1, 2, 3, \ldots$. The above values depend on the internuclear distance as well as on the directions of the electron emission, $\hat{k}_N$, and of the orientation of the molecular axis, $\hat{n}$. Thus, the reduction should be most clearly visible in a geometry with fixed directions of $\hat{k}_N$ and $\hat{n}$.

6.3. Signatures of alignment and orbital symmetry

As we have seen above, for intense-field ionization of molecules the symmetry of the electronic wavefunction of the molecule and the orientation of the molecular axis and/or plane in space appear as new parameters compared to that for the ionization of atoms. In fact
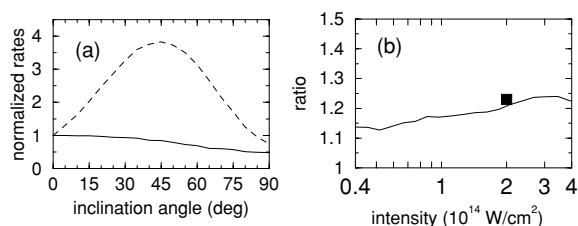
Figure 22. (a) Ionization rates of N_2 (solid line) and O_2 (dashed line) as a function of the inclination angle between the internuclear axis and the polarization axis at 800 nm and 2×10^{14} W cm^{-2} (cf [94]). (b) Ratio of ion yields for two partially aligned ensembles of molecules as a function of the laser intensity, a comparison between the prediction of the S-matrix theory (line, cf [94]) and recent experimental data (square, [126]) are shown.

detection and control of molecular alignment in intense fields is of considerable importance in photochemistry and its applications (see, e.g., recent reviews by Seideman [193], Reid [180], Stolow [199] and Stapelfeldt and Seideman [198]). Most of the experiments on molecular ionization have been performed with randomly oriented molecules. Only recently, it has become possible to measure total ion yields for ensembles of molecules showing a maximum alignment either along or perpendicular to the polarization direction [126]. The orientation dependence of field ionization of the hydrogen molecular ion has been studied theoretically by McCann and coworker [171–173]. Theoretical investigations of molecular alignment during ionization have also began.

In figure 22(a) results of the S-matrix calculations, performed by Jaroń–Becker *et al* [94], for the total ionization *rates* of N_2 (solid line) and O_2 (dashed line) as a function of the angle between the polarization direction and the molecular axis are shown. They are obtained for $\lambda = 800$ nm and an intensity of 3.2×10^{14} W cm^{-2}. The comparison shows that for N_2 the ionization rates decrease monotonically with increasing inclination angle, while those for O_2 have a maximum at about $45°$ and are at minimum for alignment along and perpendicular to the polarization axis. Similar dependence on the inclination angle in the case of N_2 has also been found by Kjeldsen and Madsen [103] using the S-matrix theory in length gauge. Qualitatively, the results for the rates as a function of the inclination angle agree with those calculated from the molecular tunneling theory by Zhao *et al* [221]. The results can be simply understood in terms of the orientation of the electronic density of the molecular ground states with respect to the field direction [221]. Thus, in a strong linearly polarized laser field the rate of ionization is expected to be maximum, if the maximum of the electronic density is aligned along the polarization direction. This is reached for alignment of the molecular axis along the polarization direction in the case of $N_2(\sigma_g$-orbital), and for an angle of about $45°$ between the molecular axis and the polarization direction for $O_2(\pi_g$-orbital).

In figure 22(b) we compare the experimental data (square) on alignment-dependent strong-field ionization of N_2, obtained by Litvinyuk *et al* [126], with the predictions [94] of the S-matrix formula (line) for $\lambda = 800$ nm, $I = 2 \times 10^{14}$ W cm^{-2} and $\tau = 40$ fs. The ratios of the ion yields for two ensembles of molecules with a maximum alignment along and perpendicular to the field direction are plotted. The theoretical results are seen to be in agreement with the experimental data (solid square) and show, quite generally, that N_2 molecules aligned along the field direction are easier to ionize than those aligned perpendicular to it.

For planar molecules, a strong dependence of the total ionization S-matrix rates on the orientation of the molecular plane with respect to the polarization direction has been found by Kjeldsen *et al* [102]. For example, for ethylene (C_2H_4) the rates were found to decrease monotonically with increase of the angle between the molecular plane and the polarization

(a) N$_2$(σ_g)

β=0°   β=30°   β=180°

ε   ε   ε

(b) O$_2$(π_g)

β=0°   β=30°   β=180°

ε   ε   ε
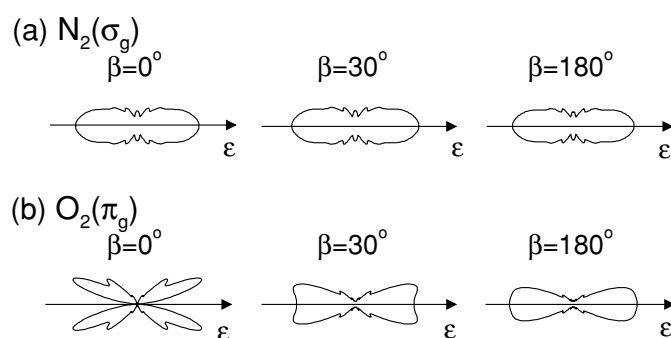
Figure 23. Comparison of photoelectron angular distributions for ionization of (a) N$_2$(σ-symmetry) and (b) O$_2$(π-symmetry) for different cone angles of alignment (cf [93]).

direction. In contrast, for benzene (C$_6$H$_6$) the orientational dependence of the rate was found to be more complex with minima appearing for the alignment of the molecular plane either parallel or perpendicular to the field direction. This has been attributed to the presence of two nodal planes in the HOMOs of benzene, one parallel and the other perpendicular to the molecular plane.

Determination of a possible alignment of an ensemble of molecules in an experiment with intense fields is a non-trivial problem. In fact, to be able to ascertain the alignment of an ensemble in the laser focus, it is necessary to find observable signatures of such alignments experimentally, preferably without having to destroy the molecule e.g. by dissociation. A non-destructive signature of alignment has been predicted using IMST, by Jaroń–Becker *et al* [93–95] and by Kjeldsen *et al* [102], which can appear in the photoelectron angular distributions and energy distributions of diatomic and/or polyatomic molecules. The origin of the signatures has been analysed and shown to lie in the symmetries of the molecular orbitals.

As an example in figure 23, we show the results of calculations [93] for the angular distributions of electrons emitted from (a) N$_2$ and (b) O$_2$, for a laser peak intensity $I_0 = 10^{14}$ W cm^{-2}, wavelength $\lambda = 800$ nm and pulse length $\tau = 10$ fs. The angle β is the cone angle of alignments as measured with respect to the polarization direction; $\beta = 0°$ corresponds to full alignment (all molecules are aligned along the polarization axis), while $\beta = 180°$ corresponds to completely random distribution of molecular axes. In the figure, polar angles are measured from the laser polarization $\hat{\epsilon}$ axis in the laboratory frame. The angular distributions clearly show a characteristic difference between the two molecules. Thus, while for N$_2$ the distributions remain essentially unchanged for any degree of alignment, for O$_2$, in contrast, a *node* appears along the polarization direction, as the cone angle of alignment β is decreased from 180° (random orientation) towards 0° (complete alignment). This behaviour is directly related to the π- or σ-symmetry of the active electronic orbital of the molecule. In O$_2$(π_g-symmetry) there is a nodal plane through the molecular axis, which leads to a vanishing photoelectron angular distribution along this axis. In a randomly oriented ensemble of molecules this minimum cannot show up due to the addition of non-zero contributions from the molecules having other orientations. But, for an aligned ensemble of linear molecules the body axes all coincide with the space-fixed axis (polarization axis) and hence the node can show up, when present, along this common axis. In contrast, in linear molecules having active orbitals of σ-symmetry there is no such nodal plane along the molecular axis, and hence the distributions also remain without a characteristic nodal structure, for any degree of alignment. From the above symmetry consideration it has been predicted that the nodal signature of alignment will appear for the class of linear diatomic molecules having active π-electrons
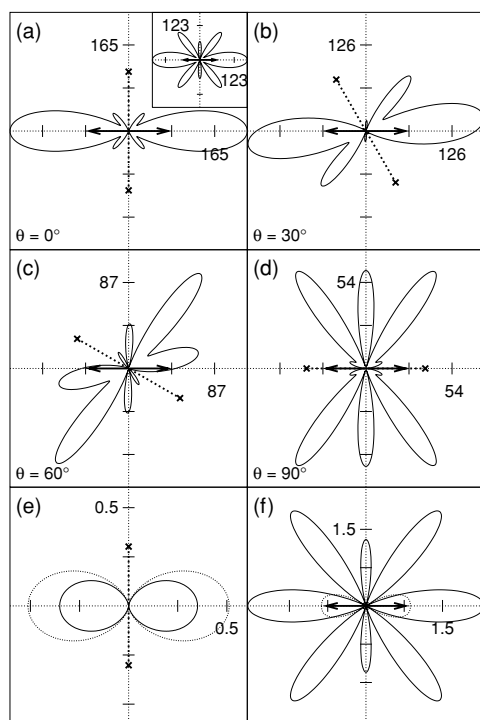
Figure 24. Comparison of angular differential ionization rates of ethylene for different orientations of the C–C axis (dotted line), (a) $\Theta = 0°$, (b) $\Theta = 30°$, (c) $\Theta = 60°$ and (d) $\Theta = 90°$. The polarization axis is horizontal (double headed arrow) and the molecular plane is perpendicular to the paper. Laser parameters: $\lambda = 800$ nm, $I = 10^{13}$ W cm^{-2} (from [102]). In the lower panels are shown: (e) the square of the Fourier transform of the initial-state wavefunction $|\tilde{\phi}_i(\boldsymbol{k}_N)|^2$, and (f) the square of the generalized Bessel function, $J_N^2(a_k, b)$, for the photon orders $n = 8$ (solid line) and $n = 9$ (dashed line). Copyright 2003 by the American Physical Society.

(as long as the contributions from inner valence shells of σ-symmetry remain small) [93, 94].

The angular distributions, or the differential ionization rates, of planar molecules, e.g. C_2H_4 and C_6H_6, have been found, as might be expected, to depend strongly on the angle between a symmetry axis of the molecule and a fixed field direction in space [102]. This is exemplified in the plots of figures 24(a)–(d) for different orientations of the C–C axis (dashed line) of ethylene molecule with respect to the field polarization direction (double headed arrow). It is seen from the figure that there are no electrons emitted along the C–C axis. More generally, the calculations show that no electrons are emitted in the molecular plane. This circumstance is due to the antisymmetry of the HOMO of ethylene with respect to a reflection in the nodal plane of the molecule.

6.4. Ionization cum vibrational excitation

Ionization of molecules in intense fields may leave the residual ion not only in the ground state but also in *vibrationally excited* states. In a recent experiment [205] it is found rather unexpectedly that the relative populations of the vibrational levels of the H_2^+ ions are concentrated in the lowest vibrational levels and do *not* follow the Franck–Condon principle. It would be of much interest therefore to investigate using IMST the probability of vibrational

excitation accompanied by ionization. To this end we give below the lowest order IMST amplitudes for such processes.

Assuming an adiabatic-nuclei approximation, the wavefunction of the νth vibrational level of the electronic orbital i can be written in the form:

$$\Phi_\nu^{(i)} = \psi_\nu(x)\Phi_i(\mathbf{r}; \mathbf{R}_1, \mathbf{R}_2, \ldots, \mathbf{R}_n) \exp\left(-\mathrm{i}E_\nu^{(i)}t\right) \tag{89}$$

with $\psi_\nu(x)$ being the vibrational wavefunction of an active mode

$$\psi_\nu(x) = \sqrt{\frac{\alpha}{\sqrt{\pi}2^\nu(\nu!)}} H_\nu(\alpha x) \exp(-\alpha^2 x^2/2), \tag{90}$$

where H_ν are the Hermite polynomials (other forms of vibrational wavefunctions, e.g. Morse-oscillator wavefunctions may also be used here, if needed). The rate of differential ionization for a transition from a vibrational level ν in the neutral molecule to the level ν' in the molecular ion can then be written as

$$\frac{\mathrm{d}W_{\nu,\nu'}(\boldsymbol{k}_N)}{\mathrm{d}\hat{\boldsymbol{k}}_N} = 2\pi C^2(Z, E_B, F)k_N(U_p - N\omega)^2 J_N^2\left(\boldsymbol{\alpha}_0 \cdot \boldsymbol{k}_N, \frac{U_p}{2\omega}\right)$$

$$\times \left|\sum_{j=1}^{p} 2\langle\phi_{\boldsymbol{k}_N}(\boldsymbol{r})|\tilde{\phi}_j(\boldsymbol{r})\rangle \begin{cases} \mathrm{Re}\big(t_{\nu,\nu'}^{(N)}\big)\Big|^2 & : \text{bonding orbital pairs} \\ \mathrm{Im}\big(t_{\nu,\nu'}^{(N)}\big)\Big| & : \text{anti-bonding orbital pairs,} \end{cases} \tag{91}$$

where

$$t_{\nu,\nu'}^{(N)} = \exp(\mathrm{i}\lambda R_e p) N(\nu, \nu') \sum_{n=0}^{\tilde{n}} (-1)^n b_n I(\nu + \nu' - 2n, p) \tag{92}$$

with

$$p = \frac{k_N}{2\lambda} \cos\theta \tag{93}$$

$$\cos\theta = \cos\theta_{k_N} \cos\theta_R + \sin\theta_{k_N} \sin\theta_R \cos(\phi_{k_N} - \phi_R) \tag{94}$$

$$N(\nu, \nu') = \sqrt{\frac{\alpha/\lambda(\nu!)}{\sqrt{\pi}2^\nu}} \sqrt{\frac{\alpha'/\lambda(\nu'!)}{\sqrt{\pi}2^{\nu'}}} (2\alpha/\lambda)^\nu (2\alpha'/\lambda)^{\nu'} \tag{95}$$

$$b_n = \left(\frac{2\alpha'}{\lambda}\right)^{-2n} \sum_{m=0}^{[\nu/2]_\mathrm{int}} \frac{(\alpha'/\alpha)^{2m}}{m!(\nu-2m)!(n-m)!(\nu-2(n-m))!} \tag{96}$$

$$\tilde{n} = \left[\frac{\nu}{2}\right]_\mathrm{int} + \left[\frac{\nu'}{2}\right]_\mathrm{int} \tag{97}$$

$$I(s, p) = \sqrt{2\pi}\,(\mathrm{i})^s \exp\left(-\frac{p^2}{2}\right) \sum_{k=0}^{[s/2]_\mathrm{int}} \frac{s!\,p^{s-2k}}{(s-2k)!k!2^k} \tag{98}$$

and R_e is the equilibrium distance between the atomic orbital pair.

7. Summary

We have reviewed the IMST, which provides a systematic *ab initio* approach to analyse intense-field processes in general, and its application to a number of problems of much current interest for interaction of atoms and molecules with intense laser radiation. The derivation of IMST and its diagrammatic representation with special reference to identification of the dominant

mechanisms in a process of interest with the help of the latter is elucidated. The structural flexibility of IMST is shown to permit introduction of any relevant intermediate (or door-way) propagator which may crucially influence a given reaction in the leading terms of the series, independently of the choice of the initial and final reference states of the transition process. The usual 'prior' and 'post' expansions of the S-matrix are shown to be reobtained as restricted special cases of IMST. Practical usefulness of IMST is illustrated by the results of applications to several ubiquitous phenomena in intense-field physics, namely single ionization of atoms and molecules, high harmonic generation as well as double and multiple ionization.

Single ionization of atoms with reference to the experimental observations and the Coulomb-corrected KFR model, optical tunnel ionization and the relation between the 'photon picture' and the 'field-ionization picture' are discussed. Results for the electron energy spectra and the phenomena associated with the rescattering mechanism are briefly discussed. The differential and the total ionization rates in the relativistic and non-relativistic theories are compared and the role of spin response of the Dirac H-atom to intense fields is briefly discussed.

A consistent quantum amplitude formulation of HHG using IMST is derived and its equivalence with the usual method of expectation value of the current is pointed out. The most general properties of HHG, including odd harmonic generation from a single atom as well as its coherent amplification by many atoms, and 'hyper-Raman emission' are discussed.

For the problem of double ionization, expressions up to the second order of IMST for the amplitude are analysed both physically as well as quantitatively. Comparison with the experimental data shows that the dominant diagram for the NSDI, in the near-infrared wavelength regime, is the 'correlated energy-sharing' (or rescattering) diagram. Predictions of IMST analysis for the recent coincidence experiments for double ionization are also discussed. Two important final-state effects are revealed to be of considerable significance from the analysis of the NSDI data: (a) the role of Volkov dressing of the electrons by the field and (b) the importance of the full inter-electron correlation. Extensions of the theory to higher orders are also indicated. A simple *model* formula for calculation of the rates of multiple ionization is discussed and tested with respect to the experimental data. The process of inner-shell ionization of atoms in intense laser field is considered and the formation of 'hollow ions' in the process is discussed.

Differential and total ionization rates of molecules are reviewed and the phenomenon of 'suppressed ionization' is discussed. It is shown that a constructive or a destructive interference effect between the sub waves of the ionizing electron arising from the atomic centres, which depend on the molecular symmetry, can significantly influence the total ionization yields of the molecule. Similar influence of molecular symmetry holds true for the *alignment* of the molecular axis with respect to the field direction. Characteristic signatures of orbital symmetry and molecular alignment in the photo-electron angular distributions, and energy distributions, are discussed. They are shown to provide a means of *non*-destructive determination of the alignment of molecular axis, induced by the laser field.

Finally, an explicit expression for the probability distribution of *vibrational* excitations accompanied by ionization in intense fields is given which is expected to help analyse the 'non-Franck–Condon distribution' observed recently in experiments that resolve the vibrational excitations following the ionization of a molecule in intense laser fields.

8. Outlook

In this concluding section, we briefly point out a few directions in which applications of IMST could lead to progress in the near future.

Single ionization of molecules reviewed here demonstrated characteristic dependence of the ionization rates on the symmetry of the molecular orbitals. But little is known so far of the role of molecular symmetry on the double ionization *and* fragmentation of molecules in intense fields. Recent experiments on double ionization [50] and fragmentation [27, 2] of molecules appear to strongly indicate the presence of the influence of such symmetries.

An important recent development in the laboratory is the availability of *ultrashort* laser pulses lasting only for a few optical cycles or for attoseconds [154, 30, 166, 5, 130]. In such short pulses a new parameter becomes important, namely the phase of the carrier wave (with respect to the envelope). The effect of the carrier-envelope phase on the direction of the photoelectron emission has been observed experimentally recently [166]. Note that the usual ionization *rate* is not an appropriate parameter for processes in such short pulses. Time-dependent probability distributions can nevertheless be obtained using the explicitly time-dependent amplitudes of IMST discussed in section 3; use of S-matrix theory in this direction has already began (see e.g. [140]).

A great majority of processes investigated experimentally and analysed using IMST (and other methods) so far relate essentially to the outer-shell electrons of the electronic systems (atoms, molecules, clusters etc). Currently we are witnessing developments of free-electron lasers (e.g. [192]) as well as of strong high-order harmonic sources (e.g. [130, 155]) delivering intense pulses in the short VUV and/or XUV wavelengths. This opens up the interesting possibility of observing intense-field processes from the *inner* shells of atoms and molecules which can be fruitfully analysed using IMST. For example, using an extension of IMST it has been recently predicted [19] that at high frequencies the two-photon inner-shell ionization rates can exceed the one-photon valence-shell ionization rates in a class of alkali atoms; e.g. the results clearly indicate that creation of hollow ions via a two-photon inner-shell ionization is very likely for K atoms. Such hollow ions (atoms) are 'inverted' objects and can give rise to laser emission (coherent amplification) at high frequencies.

Acknowledgments

References

[1]   Agostini P, Fabre F, Mainfray G, Petite G and Rahman N K 1979 *Phys. Rev. Lett.* **42** 1127
[2]   Alnaser A S *et al* 2004 *Phys. Rev. Lett.* **93** 113003
[3]   Auguste T, Monot P, Lompre L A, Mainfray G and Manus C 1992 *J. Biol. Phys.* **25** 4181
[4]   Ammosov M V, Delone N B and Krainov V P 1986 *Zh. Eksp. Teor. Fiz.* **91** 2008
      Ammosov M V, Delone N B and Krainov V P 1986 *Sov. Phys.–JETP* **64** 1191 (Engl. Transl.)
[5]   Baltuska A, Udem T, Uiberacker M, Hentschel M, Goulielmakis E, Gohle C, Yakovlev V S, Scrinzi A,
          Hänsch T W and Krausz F 2003 *Nature* **421** 611
[6]   Bandrauk A D (ed) 1994 *Molecules in Laser Fields* (New York: Marcel Dekker)
[7]   Bandrauk A D, Chelkowski S and Kawata I 2003 *Phys. Rev.* A **67** 013407
[8]   Becker A and Faisal F H M 1994 *Phys. Rev.* A **50** 3256
      Becker A and Faisal F H M 1995 *Phys. Rev.* A **51** 3390 (erratum)
[9]   Becker A and Faisal F H M 1996 *J. Phys. B: At. Mol. Opt. Phys.* **29** L197
[10] Becker A and Faisal F H M 1999 *Phys. Rev.* A **59** R1742
[11] Becker A and Faisal F H M 1999 *Phys. Rev.* A **59** R3182
[12] Becker A and Faisal F H M 1999 *J. Phys. B: At. Mol. Opt. Phys.* **32** L335

[13] Becker A and Faisal F H M 2000 *Phys. Rev. Lett.* **84** 3546
[14] Becker A, Faisal F H M, Liang Y, Augst S, Beaudoin Y, Chaker M and Chin S L 2000 *J. Phys. B: At. Mol. Opt. Phys.* **33** L547
[15] Becker A, Plaja L, Moreno P, Nurhuda M and Faisal F H M 2001 *Phys. Rev.* A **64** 023408
[16] Becker A and Faisal F H M 2001 *Opt. Exp.* **8** 383
[17] Becker A, Bandrauk A D and Chin S L 2001 *Chem. Phys. Lett.* **343** 345
[18] Becker A and Faisal F H M 2002 *Phys. Rev. Lett.* **89** 193003
[19] Becker A and Faisal F H M 2003 *Laser Phys.* **13** 430
[20] Becker W, Long S and McIver J K 1990 *Phys. Rev.* A **41** 4112
[21] Becker W, Lohr A and Kleber M 1994 *J. Phys. B: At. Mol. Opt. Phys.* **27** L325
[22] Becker W, Lohr A and Kleber M 1995 *Quantum Semiclass. Opt.* **7** 423
[23] Becker W, Lohr A, Kleber M and Lewenstein M 1997 *Phys. Rev.* A **56** 645
[24] Becker W, Grasbon F, Kopold R, Milosevic D B, Paulus G G and Walther H 2002 *Adv. At. Mol. Opt. Phys.* **48** 35
[25] Bender C M and Orszag S A 1978 *Advanced Mathematical Methods for Scientists and Engineers* (New York: McGraw-Hill)
[26] Berestetskii V B, Lifshitz E M and Pitaevskii L P 1971 *Relativistic Quantum Theory* (Oxford: Pergamon)
[27] Bhardwaj V R, Rayner D M, Villeneuve D M and Corkum P B 2001 *Phys. Rev. Lett.* **87** 253003
[28] Borca B, Frolov M V, Manakov N L and Starace A F 2002 *Phys. Rev. Lett.* **88** 193001
[29] Brabec T, Ivanov M Yu and Corkum P B 1996 *Phys. Rev.* A **54** R2551
[30] Brabec T and Krausz F 2000 *Rev. Mod. Phys.* **72** 545
[31] Bunkin F B, Kazakov A E and Fedorov M V 1972 *Usp. Fiz. Nauk.* **107** 559
      Bunkin F B, Kazakov A E and Fedorov M V 1972 *Sov. Phys. Usp.* **15** 416 (Engl. Transl.)
[32] Chaloupka J L, Rudati J, Lafon R, Agostini P, Kulander K C and DiMauro L F 2003 *Phys. Rev. Lett.* **90** 033002
[33] Charalambidis D, Xenakis D, Uiterwaal C J G J, Maragakis P, Jian Zhang, Schröder H, Faucher O and Lambropoulos P 1997 *J. Phys. B: At. Mol. Opt. Phys.* **30** 1467
[34] Chen B, Faisal F H M, Jeztke S, Lutz H O and Scanzano P 1987 *Phys. Rev.* A **36** 4091
[35] Chin S L, Liang Y, Decker J E, Ilkov F A and Ammosov M V 1992 *J. Phys. B: At. Mol. Opt. Phys.* **25** L249
[36] Chu Shi-I and Reinhardt W P 1977 *Phys. Rev. Lett.* **39** 1195
[37] Chu S and Telnov D A 2004 *Phys. Rep.* **390** 1
[38] Corkum P B 1993 *Phys. Rev. Lett.* **71** 1994
[39] Cornaggia C and Hering Ph 1998 *J. Phys. B: At. Mol. Opt. Phys.* **31** L503
[40] Crawford D P and Reiss H R 1994 *Phys. Rev.* A **50** 1844
[41] Crawford D P and Reiss H R 1998 *Opt. Exp.* **2** 289
[42] Demkov Yu N and Drukarev G F 1964 *Zh. Eksp. Teor. Fiz.* **47** 918
      Demkov Yu N and Drukarev G F 1965 *Sov. Phys.–JETP* **20** 614 (Engl. Transl.)
[43] DeWitt M J, Wells E and Jones R R 2001 *Phys. Rev. Lett.* **87** 153001
[44] Dimou L and Faisal F H M 1987 *Phys. Rev. Lett.* **59** 872
[45] Dörner R, Weber Th, Weckenbrock M, Staudte A, Hattass M, Moshammer R, Ullrich J and Schmidt-Böcking H 2002 *Adv. At. Mol. Phys.* **48** 1
[46] Eberly J H, Su Q and Javanainen J 1989 *Phys. Rev. Lett.* **62** 881
[47] Ehlotzky F, Jaroń A and Kamiński J Z 1998 *Phys. Rep.* **297** 63
[48] Ehlotzky F 2001 *Phys. Rep.* **345** 175
[49] Eichmann U, Dörr M, Maeda H, Becker W and Sandner W 2000 *Phys. Rev. Lett.* **84** 3550
[50] Eremina E, Liu X, Rottke R, Sandner W, Schätzel M G, Dreischuh A, Paulus G G, Walther H, Moshammer R and Ullrich J 2004 *Phys. Rev. Lett.* **92** 173001
[51] Faisal F H M 1970 *J.Phys. B: At. Mol. Phys.* **3** 636
[52] Faisal F H M and Tench A V L 1971 *Comput. Phys. Commun.* **2** 261
[53] Faisal F H M 1973 *J. Phys. B: At. Mol. Phys.* **6** L89
[54] Faisal F H M 1976 *Nuovo Cimento* B **8** 3078
[55] Faisal F H M 1987 *Theory of Multiphoton Processes* (New York: Plenum)
[56] Faisal F H M 1987 *Phys. Lett.* A **119** 375
[57] Faisal F H M 1987 *Phys. Lett.* A **125** 200
[58] Faisal F H M 1989 *Comput. Phys. Rep.* **9** 55
[59] Faisal F H M, Scanzano P and Zaremba J 1989 *J. Phys. B: At. Mol. Opt. Phys.* **22** L183
[60] Faisal F H M 1990 *Atoms in Strong Fields* (*NATO ASI Series* vol 212) ed C A Nicolaides, M Nayfeh and C Clark (New York: Plenum) p 407

[61] Faisal F H M 1990 *BiBoS (Forschungszentrum Bielefeld-Bochum Statistik) Preprint* Nr. BI-TP 90/31 (Universität Bielefeld, Bielefeld)

[62] Faisal F H M and Scanzano P 1991 *Comput. Phys. Commun.* **63** 265

[63] Faisal F H M 1991 *Radiation Effects and Defects in Solids* vol 122–123 (London: Gordon and Breach) pp 27–50

[64] Faisal F H M 1994 *Phys. Lett.* A **187** 180

[65] Faisal F H M and Becker A 1996 *Selected Topics on Electron Physics* ed D H Campbell and H Kleinpoppen (New York: Plenum) p 397

[66] Faisal F H M and Becker A 1997 *Multiphoton Processes 1996* (*IOP Conference Series* vol 154) ed P Lambropoulos and H Walther (Bristol: Institute of Physics Publishing) p 118

[67] Faisal F H M and Becker A 1999 *Commun. Mod. Phys.* D **1** 15

[68] Faisal F H M, Becker A and Muth-Böhm J 1999 *Laser Phys.* **9** 115

[69] Faisal F H M and Bhattacharyya 2004 *Phys. Rev. Lett.* **93** 053002

[70] Faisal F H M in preparation

[71] Ferray M, L'Hullier A, Li X F, Lompré L A, Mainfray G and Manus C 1988 *J. Phys. B: At. Mol. Opt. Phys.* **21** L31

[72] Feuerstein B *et al* 2001 *Phys. Rev. Lett.* **87** 043003

[73] Figueira de Morisson Faria C, Schomerus H and Becker W 2002 *Phys. Rev.* A **66** 043413

[74] Figueira de Morisson Faria C, Liu X, Becker W and Schomerus H 2004 *Phys. Rev.* A **69** 021402(R)

[75] Figueira de Morisson Faria C, Schomerus H, Liu X and Becker W 2004 *Phys. Rev.* A **69** 043405

[76] Fittinghoff D N, Bolton P R, Chang B and Kulander K C 1992 *Phys. Rev. Lett.* **69** 2642

[77] Fisher V, Ralchenko Yu, Goldgrish A, Fisher D and Maron Y 1995 *J. Phys. B: At. Mol. Opt. Phys.* **28** 3027

[78] Gazibegović-Busuladžić A, Milošević D B and Becker W 2004 *Phys. Rev.* A **70** 053403

[79] Getzlaff M, Heidemann B, Bansmann J, Westphal C and Schönhense 1998 *Rev. Sci. Instrum.* **69** 3913

[80] Gibson G N, Freeman R R and McIllrath T J 1991 *Phys. Rev. Lett.* **67** 1230

[81] Goreslavskii S P, Popruzhenko S V, Kopold R and Becker W 2001 *Phys. Rev.* A **64** 053402

[82] Grasbon F, Paulus G G, Chin S L, Walther H, Muth-Böhm J, Becker A and Faisal F H M 2001 *Phys. Rev.* A **63** 041402(R)

[83] Guo C, Li M, Nibarger J P and Gibson G N 1998 *Phys. Rev.* A **58** R4271

[84] Hankin S M, Villeneuve D M, Corkum P B and Rayner D M 2000 *Phys. Rev. Lett.* **84** 5082

[85] Hankin S M, Villeneuve D M, Corkum P B and Rayner D M 2001 *Phys. Rev.* A **64** 013405

[86] Harris F E and Michels H H 1965 *J. Chem. Phys.* **43** 165

[87] Huramiya K, Kono H, Fujimura Y, Kawata I and Bandrauk A D 2002 *Phys. Rev.* A **66** 043403

[88] Hentschel M, Kienberger R, Spielmann Ch, Reider G A, Milosevic N, Brabec T, Corkum P B, Heinzmann U, Drescher M and Krausz F 2001 *Nature* **414** 509

[89] Itzykson C and Zuber J B 1980 *Quantum Field Theory* (London: McGraw-Hill)

[90] Jain M and Tzoar N 1978 *Phys. Rev.* A **18** 538

[91] Jaroń A, Kamiński J Z and Ehlotzky F 1999 *Opt. Commun.* **163** 115

[92] Jaroń A and Becker A 2003 *Phys. Rev.* A **67** 035401

[93] Jaroń-Becker A, Becker A and Faisal F H M 2003 *J. Phys. B: At. Mol. Opt. Phys.* **36** L375

[94] Jaroń-Becker A, Becker A and Faisal F H M 2004 *Phys. Rev.* A **69** 023410

[95] Jaroń-Becker A, Becker A and Faisal F H M 2004 *Laser Phys.* **14** 179

[96] Joachain C J 1984 *Quantum Collision Theory* (Amsterdam: North Holland)

[97] Joachain C J, Dörr M and Kylstra N J 2000 *Adv. At. Mol. Opt. Phys.* **42** 225

[98] Kamiński J Z 1987 *Phys. Lett.* A **120** 396

[99] Kamiński J Z, Jaroń A and Ehlotzky F 1996 *Phys. Rev.* A **53** 1756

[100] Keldysh L V 1964 *Zh. Eksp. Teor. Fiz.* **47** 1945
       Keldysh L V 1964 *Sov. Phys.–JETP* **20** 1307 (Engl. Transl.)

[101] Kiyan I Yu and Helm H 2003 *Phys. Rev. Lett.* **90** 183001

[102] Kjeldsen T K, Bisgaard C Z, Madsen L B and Stapelfeldt H 2003 *Phys. Rev.* A **68** 063407

[103] Kjeldsen T K and Madsen L B 2004 *J. Phys. B: At. Mol. Opt. Phys.* **37** 2033

[104] Kondo K, Sagisaka A, Tamida T, Nabekawa Y and Watanabe S 1993 *Phys. Rev.* A **48** R2531

[105] Kopold R and Becker W 1999 *J. Phys. B: At. Mol. Opt. Phys.* **32** L419

[106] Kopold R, Milošević D B and Becker W 2000 *Phys. Rev. Lett.* **84** 3831

[107] Kopold R, Becker W and Kleber M 2000 *Opt. Commun.* **179** 39

[108] Kopold R, Becker W, Rottke H and Sandner W 2000 *Phys. Rev. Lett.* **85** 3781

[109] Kopold R, Becker W, Kleber M and Paulus G G 2002 *J. Phys. B: At. Mol. Opt. Phys.* **35** 217

[110] Krainov V P 1997 *J. Opt. Soc. Am.* B **14** 425

[111] Krekora P, Su Q and Grobe R 2004 *Phys. Rev. Lett.* **92** 040406
[112] Kuchiev M Yu 1987 *Pis'ma Zh. Esp. Teor. Fiz.* **45** 319
      Kuchiev M Yu 1987 *Sov. Phys.–JETP Lett.* **45** 404 (Engl. Transl.)
[113] Kuchiev M Yu 1995 *J. Phys. B: At. Mol. Opt. Phys.* **28** 5093
[114] Kuchiev M Yu 1995 *Phys. Lett.* A **212** 77
[115] Kuchiev M Yu and Ostrovsky V N 1999 *J. Phys. B: At. Mol. Opt. Phys.* **32** L189
[116] Kuchiev M Yu and Ostrovsky V N 1999 *Phys. Rev.* A **59** 2844
[117] Kuchiev M Yu and Ostrovsky V N 1999 *Phys. Rev.* A **60** 3111
[118] Kuchiev M Yu and Ostrovsky V N 2001 *J. Phys. B: At. Mol. Opt. Phys.* **34** 405
[119] Kulander K C 1988 *Phys. Rev.* A **38** 778
[120] Lafon R, Chaloupka J L, Sheehy B, Paul P M, Agostini P, Kulander K C and DiMauro L F 2001 *Phys. Rev. Lett.* **86** 2762
[121] Larochelle S, Talebpour A and Chin S L 1998 *J. Phys. B: At. Mol. Opt. Phys.* **31** 1201
[122] Lewenstein M, Balcou Ph, Ivanov M Yu, L'Huillier A and Corkum P B 1994 *Phys. Rev.* A **49** 2117
[123] Lewenstein M, Kulander K C, Schafer K J and Bucksbaum P H 1994 *Phys. Rev.* A **51** 1495
[124] L'Huillier A, Lompré L A, Mainfray G and Manus C 1982 *Phys. Rev. Lett.* **48** 1814
[125] L'Huillier A, Lompré L A, Ferray M, Mainfray G and Manus C 1988 *Europhys. Lett.* **5** 601
[126] Litvinyuk I V, Lee K F, Dooley P W, Rayner D M, Villeneuve D M and Corkum P B 2003 *Phys. Rev. Lett.* **90** 233003
[127] Lohr A, Kleber M, Kopold R and Becker W 1997 *Phys. Rev.* A **55** R4003
[128] Lotz W 1968 *Z. Phys.* **216** 241
[129] Maeda H, Dammasch M, Eichmann U, Sandner W, Becker A and Faisal F H M 2000 *Phys. Rev.* A **62** 035402
[130] Mairesse Y *et al* 2003 *Science* **302** 1540
[131] Manakov N L and Rapoport L P 1975 *Zh. Eksp. Teor. Fiz.* **69** 842
      Manakov N L and Rapoport L P 1975 *Sov. Phys.–JETP* **42** 430 (Engl. Transl.)
[132] Manakov N L, Frolov M V, Borca B and Starace A F 2003 *J. Phys. B: At. Mol. Opt. Phys.* **36** R49
[133] Maquet A, Chu Shi-I and Reinhardt W P 1983 *Phys. Rev.* A **27** 2946
[134] McGuire J H 1997 *Electronic Correlation Dynamics in Atomic Collisions* (Cambridge, UK: Cambridge University Press)
[135] McPherson A, Gibson G, Jara H, Johann U, Luk T S, McIntyre I, Boyer K and Rhodes C K 1987 *J. Opt. Soc. Am.* B **4** 595
[136] Milošević D B and Ehlotzky F 1998 *Phys. Rev.* A **57** 5002
[137] Milošević D B and Ehlotzky F 1998 *J. Phys. B: At. Mol. Opt. Phys.* **31** 4149
[138] Milošević D B and Ehlotzky F 1998 *Phys. Rev.* A **58** 3124
[139] Milošević D B and Ehlotzky F 1999 *J. Phys. B: At. Mol. Opt. Phys.* **32** 1585
[140] Milošević D B, Paulus G G and Becker W 2002 *Phys. Rev. Lett.* **89** 153001
[141] Milosevic N, Krainov V P and Brabec Th 2002 *Phys. Rev. Lett.* **89** 193001
[142] Milošević D B and Ehlotzky F 2003 *Adv. At. Mol. Opt. Phys.* **49** 373
[143] Milošević D B, Gazibegović-Busuladžić A and Becker W 2003 *Phys. Rev.* A **68** 050702
[144] Moshammer R *et al* 2000 *Phys. Rev. Lett.* **84** 447
[145] Moshammer R *et al* 2002 *Phys. Rev.* A **65** 035401
[146] Moshammer R and Rottke H private communications
[147] Mourou G A, Barty C P J and Perry M D 1998 *Phys. Today* **51** 22
[148] Muller H G, Tip A and van der Wiel M J 1983 *J. Phys. B: At. Mol. Phys.* **16** L679
[149] Muller H G 1999 *Phys. Rev.* A **60** 1341
[150] Muller H G 2001 *Opt. Exp.* **8** 425
[151] Muth-Böhm J, Becker A and Faisal F H M 2000 *Phys. Rev. Lett.* **85** 2280
[152] Muth-Böhm J, Becker A, Chin S L and Faisal F H M 2001 *Chem. Phys. Lett.* **337** 313
[153] Nikishov A I and Ritus V I 1966 *Sov. Phys.—JETP* **23** 168
[154] Nisoli M, De Silvestri S, Svelto O, Szipcs R, Ferencz K, Spielmann Ch, Sartania S and Krausz F 1997 *Opt. Lett.* **22** 522
[155] Nisoli M, Sansone G, Stagira S De Silvestri S, Vozzi C, Pascolini M, Poletto L, Villoresi P and Tondello G 2003 *Phys. Rev. Lett.* **91** 213905
[156] Nurhuda M and Faisal F H M 1999 *Phys. Rev.* A **60** 3125
[157] Papadogiannis D A, Witzel B, Kalpouzos C and Charalambidis D 1999 *Phys. Rev. Lett.* **83** 4289
[158] Panek P, Kaminski J Z and Ehlotzky F 2002 *Phys. Rev.* A **65** 033408
[159] Panek P, Kaminski J Z and Ehlotzky F 2004 *Phys. Rev.* A **69** 013404
[160] Parker J, Taylor K T, Clark C W and Blodgett-Fort S 1996 *J. Phys. B: At. Mol. Opt. Phys.* **29** L33

[161] Parker J S, Doherty B J S, Meharg K J and Taylor K T 2003 *J. Phys. B: At. Mol. Opt. Phys.* **36** L393
[162] Paul P M, Toma E S, Breger P, Mullot G, Augé, Balcou Ph, Muller H G and Agostini P 2001 *Science* **292** 1689
[163] Paulus G G, Zacher F, Walther H, Lohr A, Becker W and Kleber M 1998 *Phys. Rev. Lett.* **80** 484
[164] Paulus G G, Grasbon F, Dreischuh A, Walther H, Kopold R and Becker W 2000 *Phys. Rev. Lett.* **84** 3791
[165] Paulus G G, Grasbon F, Walther H, Kopold R and Becker W 2001 *Phys. Rev.* A **64** 021401(R)
[166] Paulus G G, Grasbon F, Walther H, Villoresi P, Nisoli M, Stagira S, Priori E and De Silvestri S 2001 *Nature* **414** 182
[167] Perelomov A M, Popov S V and Terent'ev M V 1966 *Sov. Phys.–JETP* **23** 924
[168] Perry M D, Szöke A, Landen O L and Campbell E M 1988 *Phys. Rev. Lett.* **60** 1270
[169] Perry M D, Landen O L, Szöke A and Campbell E M 1988 *Phys. Rev.* A **37** 747
[170] Peterson E R and Bucksbaum P H 2001 *Phys. Rev.* A **64** 053405
[171] Plummer M and McCann J F 1996 *J. Phys. B: At. Mol. Opt. Phys.* **29** 4625
[172] Plummer M and McCann J F 1997 *J. Phys. B: At. Mol. Opt. Phys.* **30** L401
[173] Plummer M, McCann J F and Madsen L B 1998 *Comput. Phys. Commun.* **114** 94
[174] Popruzhenko S V and Goreslavskii S V 2001 *J. Phys. B: At. Mol. Opt. Phys.* **34** L239
[175] Popruzhenko S V, Korneev Ph A, Goreslavskii S V and Becker W 2002 *Phys. Rev. Lett.* **89** 023001
[176] Posthumus J (ed) 2001 *Molecules and Cluster in Intense Laser Fields* (Cambridge: Cambridge University Press)
[177] Posthumus J H 2004 *Rep. Prog. Phys.* **67** 623
[178] Potvliege R M and Shakeshaft R 1988 *Phys. Rev.* A **38** 1098
[179] Potvliege R M and Shakeshaft R 1992 *Adv. At. Mol. Opt. Phys. Suppl.* **1** 373
[180] Reid K L 2003 *Annu. Rev. Phys. Chem.* **54** 398
[181] Reiss H R 1980 *Phys. Rev.* A **22** 1786
[182] Reiss H R 1980 *J. Opt. Soc. Am.* B **7** 574
[183] Reiss H R 1992 *Prog. Quantum Electron.* **16** 1
[184] Reiss H R 2002 *Phys. Rev.* A **65** 055405
[185] Requate A, Becker A and Faisal F H M 2003 *Phys. Lett.* A **319** 145
[186] San Roman J S, Roso L and Reiss H R 2000 *J. Phys. B: At. Mol. Opt. Phys.* **33** 1869
[187] Roman J S, Plaja L and Roso L 2001 *Phys. Rev.* A **64** 063402
[188] Salières P, L'Huillier A, Antoine Ph and Lewenstein M 1999 *Adv. At. Mol. Opt. Phys.* **41** 83
[189] Saliéres P *et al* 2001 *Science* **292** 902
[190] Schafer K J, Yang B, DiMauro L F and Kulander K C 1993 *Phys. Rev. Lett.* **70** 1599
[191] Schmidt M W *et al* 1993 *J. Comput. Chem.* **14** 1347
[192] Schulz J, Wabnitz H, Laarmann T, Gürtler P, Laasch W, Swirderski A, Möller Th and de Castro A H B 2003 *Nucl. Instrum. Methods* A **507** 572
[193] Seideman T 2002 *Annu. Rev. Phys. Chem.* **53** 41
[194] Shakeshaft R 1983 *Phys. Rev.* A **28** 667
[195] Shakeshaft R, Potvliege R M, Dörr M and Cooke W E 1990 *Phys. Rev.* A **42** 1656
[196] Shore B W and Knight P L 1987 *J. Phys. B: At. Mol. Phys.* **20** 413
[197] Smirnov B M and Chibisov M I 1965 *Zh. Eksp. Teor. Fiz.* **49** 841
      Smirnov B M and Chibisov M I 1966 *Sov. Phys.–JETP* **22** 585 (Engl. Transl.)
[198] Stapelfeldt H and Seideman T 2003 *Rev. Mod. Phys.* **75** 543
[199] Stolow A 2003 *Annu. Rev. Phys. Chem.* **54** 89
[200] Szymanowski C, Veniard V, Taïeb R and Maquet A 1997 *Phys. Rev.* A **56** 3846
[201] Talebpour A, Chien C-Y and Chin S L 1996 *J. Phys. B: At. Mol. Opt. Phys.* **29** L677
[202] Talebpour A, Larochelle S and Chin S L 1998 *J. Phys. B: At. Mol. Opt. Phys.* **31** L49
[203] Talebpour A, Bandrauk A D, Yang J and Chin S L 1999 *Chem. Phys. Lett.* **313** 789
[204] Tong X M, Zhao Z X and Lin C D 2002 *Phys. Rev.* A **66** 033402
[205] Urbain X, Fabre B, Staicu-Casagrande E M, de Ruette N, Andrianarijaona V M, Jureta J, Posthumus J H, Saenz A, Baldit E and Cornaggia C 2004 *Phys. Rev. Lett.* **92** 163004
[206] Volkov D M 1935 *Z. Phys.* **94** 250
[207] Walser M W, Urbach D J, Hatsagortsyan K Z, Hu S X and Keitel C H 2002 *Phys. Rev.* A **65** 043410
[208] Walker B, Sheehy B, DiMauro L F, Agostini P, Schafer K J and Kulander K C 1994 *Phys. Rev. Lett.* **73** 1227
[209] Walsh T D G, Decker J E and Chin S L 1994 *J. Phys. B: At. Mol. Opt. Phys.* **26** L85
[210] Walsh T D G, Ilkov F A, Decker J E and Chin S L 1994 *J. Phys. B: At. Mol. Opt. Phys.* **27** 3767
[211] Weber T *et al* 2000 *Phys. Rev. Lett.* **84** 443
[212] Weber Th, Giessen H, Weckenbrock M, Staudte A, Spielberger L, Jagutzki O, Mergel V, Urbasch G, Vollmer M and Dörner R 2000 *Nature* **405** 658

[213] Weber Th *et al* 2000 *J. Phys. B: At. Mol. Opt. Phys.* **33** L127
[214] Weckenbrock M, Hattass M, Czasch A, Jagutzki O, Schmidt L, Weber Th, Roskos H, Löffler T, Thomson M and Dörner R 2001 *J. Phys. B: At. Mol. Opt. Phys.* **34** L449
[215] Weckenbrock M, Becker A, Staudte A, Kammer S, Smolarski M, Bhardwaj V R, Rayner D M, Villeneuve D M, Corkum P B and Dörner R 2003 *Phys. Rev. Lett.* **91** 123004
[216] Weckenbrock M *et al* 2003 *Phys. Rev. Lett.* **92** 213002
[217] Wells E, DeWitt M J and Jones R R 2002 *Phys. Rev.* A **66** 013409
[218] Witzel B, Papadogiannis N A and Charalambidis D 2000 *Phys. Rev. Lett.* **85** 2268
[219] Yamakawa K, Akahane Y, Fukuda Y, Aoyama M, Inoue N, Ueda H and Utsumi T 2004 *Phys. Rev. Lett.* **92** 123001
[220] Yudin G L and Ivanov M Yu 2001 *Phys. Rev.* A **63** 033404
[221] Zhao Z X, Tong X M and Lin C D 2003 *Phys. Rev.* A **67** 043404